Atomic networks as highways for holes in oxygen-deficient amorphous oxides

Rafael Costa-Amaral*,† and Yu Kumagai*,†,‡

†Institute for Materials Research, Tohoku University, Sendai 980-8577, Japan. ‡Organization for Advanced Studies, Tohoku University, Sendai 980-8577, Japan

E-mail: costa.amaral.rafael@gmail.com; yukumagai@tohoku.ac.jp

Abstract

Oxygen-deficient amorphous tellurium oxides $(a\text{-TeO}_x)$ have recently challenged the intrinsic hole mobility limits of amorphous oxides, with thin-film transistors reaching mobilities up to $15\,\mathrm{cm}^2\,\mathrm{V}^{-1}\,\mathrm{s}^{-1}$ upon Se doping. However, the atomistic origins of this behavior, and its seeming contradiction with established semiconductor physics, have remained unresolved. Here, we combine machine-learning-accelerated *ab initio* molecular dynamics with hybrid-functional defect calculations to establish a new microscopic picture. We show that substantial oxygen loss drives spontaneous segregation into interpenetrating a-Te and $a\text{-TeO}_2$ domains, rather than forming dispersed oxygen vacancies. The diffuse Te-5p states from the a-Te network supply percolative pathways for holes, so mobility rises monotonically with oxygen deficiency, enabling mobilities that exceed current records. Doped Se incorporates into the a-Te domain, enhancing the connectivity of conductive pathways, thereby increasing hole mobility. Similar behavior in amorphous SeO $_x$ suggests domain percolation as a general route to high-mobility p-type transport in amorphous oxides.

Keywords: p-type amorphous oxides, Hole transport mechanism, Tellurium oxides, Oxygen-

Introduction

Amorphous oxide semiconductors are promising for next-generation complementary metal-oxide-semiconductor technologies and large-area electronics as they can be deposited uniformly at low temperatures with scalable, cost-efficient methods. 1,2 While n-type materials such as amorphous InGaZnO (a-IGZO) have achieved commercial success, 3,4 the development of high-mobility p-type oxides remains a challenge, limited by deep, localized valence-band states from anisotropic oxygen 2p orbitals. Designing oxides whose valence-band maximum (VBM) is lifted and delocalized through hybridization with cationic d^{10} or s^2 lone-pair orbitals has yielded promising crystalline materials, such as Cu_2O , 5 CuAlO_2 , 6 SnO, 7 K_2SnO_2 , 8 and BaBiO_3 . 9 However, they often face limitations in mobility, stability, or manufacturability, preventing them from displacing industry-standard B-doped amorphous silicon (a-Si:H).

Recently, thin-film transistors (TFTs) based on selenium-doped oxygen-deficient amorphous tellurium oxides have delivered hole mobilities up to $15\,\mathrm{cm^2\,V^{-1}\,s^{-1}}$, 10 performing well beyond typical amorphous oxides. However, the origin of their intrinsic p-type conductivity and transport properties remains elusive. Conventional band-alignment and point-defect calculations predict that crystalline tellurium oxides should be wide-gap, hard-to-dope insulators, 11,12 while oxygen vacancies, the dominant defect in oxygen-poor films, act as deep donors that counteract p-type conduction. 13,14 Selenium, although beneficial for mobility, has been reported to introduce n-type doping, 10 further clouding the picture. The atomic model proposed in the previous study, based on a disordered matrix with dispersed oxygen vacancies, proves difficult to reconcile with spectroscopic signatures indicating the presence of elemental Te. 10 Competing hypotheses 15 that oxygen vacancies create "shallow acceptors" likewise contradict both defect physics and prior results for crystalline TeO₂. 11,12 Clarifying

these inconsistencies requires an original atomistic picture that reconciles structural and electronic observations and establishes the fundamental mechanism of hole conduction in this unusual amorphous oxide.

Here, we propose a new atomistic model for oxygen-deficient amorphous tellurium oxides $(a\text{-TeO}_x)$ using machine-learning-accelerated ab-initio molecular dynamics (AIMD) and hybrid-functional defect calculations across compositions x=0.0–2.0, including the stoichiometry used in devices. ¹⁰ In the dilute limit, oxygen vacancies unequivocally behave, just as in the crystals, ^{11,12} as high-energy deep donors, failing to explain the observed p-type conductivity. Instead, we find that substantial oxygen deficiency drives spontaneous phase segregation into interpenetrating amorphous Te and TeO₂ networks, consistent with spectroscopic evidence of elemental Te in the films. ¹⁰ Neutral Te supplies shallow, delocalized 5p states that create percolative pathways for holes, and the volume fraction of this metallic sub-network, and thus the hole mobility scales with oxygen deficiency.

This model also rationalizes the three-fold mobility boost obtained with Se doping: our simulations show that Se preferentially incorporates into the Te domains, extending the conductive network without introducing deep traps. Because the mobility gain is accompanied by band-gap narrowing, our results expose a tunable mobility-band-gap trade-off that can be engineered through the oxygen chemical potential or co-evaporation of TeO_2/Te . Calculations on amorphous SeO_x suggest that this percolation-assisted transport mechanism may constitute a general strategy for unlocking high-mobility p-type amorphous oxides.

Results and Discussion

Figure 1a displays the crystalline bonding environments in elemental and oxidized tellurium. Elemental Te, having preference for twofold coordination, 16 crystallizes as helical chains held together by van-der-Waals and dipole interactions, yielding hole mobilities approaching $790 \,\mathrm{cm}^2 \,\mathrm{V}^{-1} \,\mathrm{s}^{-1}$. At each Te atom, the lone pairs point outward into free space. Oxidation

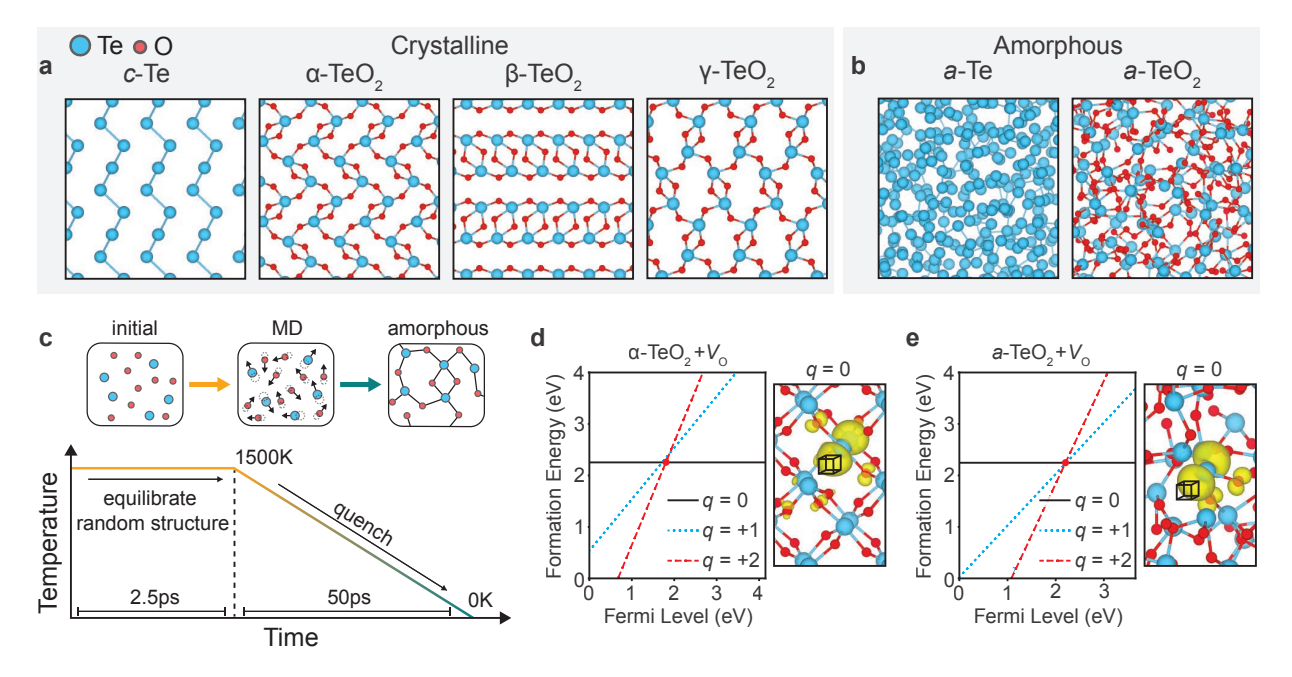


Figure 1: Atomic structures and oxygen-vacancy energetics in crystalline and amorphous TeO₂. (a) Reference crystalline phases: trigonal tellurium (c-Te) and the polymorphs α -, β - and γ -TeO₂. Te atoms are displayed in blue, O atoms in red. (b) Amorphous counterparts obtained by melt-and-quench molecular-dynamics simulations for elemental Te (a-Te) and TeO₂ (a-TeO₂). (c) Schematic of the melt-and-quench protocol used to generate the amorphous structures from random initial configurations. (d,e) Formation energies of oxygen vacancies (V_O) in (d) α -TeO₂ and (e) a-TeO₂ as a function of the Fermi level (referenced to the VBM) ranging from zero up to the conduction-band minimum. Typical three charge states, q = 0 (solid line), +1 (dotted) and +2 (dashed), in O-rich conditions are considered. The relaxed defect geometries are also depicted, where the vacancies are indicated by cubes, with the associated charge-density isosurfaces (in yellow) of the donor states at q = 0. The isosurfaces are set to 10 % of the maximum value each.

to tellurium dioxide (TeO₂) produces three well-known polymorphs, the α , β and γ phases, in which four-coordinated Te⁴⁺ centers adopt distorted trigonal bipyramids with a lone-pair-vacated site. Amorphous TeO₂ (a-TeO₂), in Figure 1b, can therefore be viewed as a random mixture of these polyhedra, preserving the local motifs.

Oxygen vacancies are the primary manifestation of oxygen deficiency in oxides and typically behave as donor defects that suppress p-type transport. 13,14 Their role in amorphous oxides is less clear, because the notion of a well-defined point defect blurs, 18,19 resulting in unconventional behavior such as enabling hole-hopping conduction pathways, as observed in a-TiO₂. 19 Thus, we initially compared the formation energies of oxygen vacancies and

their charge-transition levels in crystalline α -TeO₂, the ground state, ²⁰ and in a-TeO₂. As the three non-equivalent O sites sampled in the glass exhibit similar formation energies, see Figure S1 of the Supporting Information, we showcase the lowest-energy configuration.

In both crystalline and amorphous phases, the oxygen vacancies introduce mid-gap transition levels (Figure 1d,e), confirming they are very deep donors whose electrons are trapped by adjacent Te-5p orbitals, in line with prior results for β -TeO₂. ^{11,12} Therefore, the recently reported shallow acceptor behavior of oxygen vacancies ¹⁵ likely reflects occupied vacancy states near the valence band. The open, lone-pair network of a-TeO₂ inhibits stabilization via M-M dimerization, unlike in a-Al₂O₃, ¹⁸ keeping the neutral-vacancy formation energy high, around 2.3 eV, similar to the crystalline phase. Hence, oxygen vacancies in tellurium oxides are different from those acting as shallow donors in oxides such as WO₃, ²¹ In₂O₃, ²² or MgIn₂O₄. ²³ They neither generate n-type conductivity nor explain the hole transport observed experimentally, instead pinning the Fermi level roughly 0.7–1.1 eV above the VBM. These findings rule out sparse vacancies as the origin of conductivity and motivate exploration of alternative mechanisms for accommodating oxygen deficiency.

The amorphous structures were generated by quenching pre-equilibrated randomly initialized structures from 1500 K to 0 K via AIMD (Figure 1c), using the r²SCAN meta-GGA²⁴ for the dynamics and the HSE06^{3,4} hybrid functional for subsequent structural and electronic refinements (full details in Methods and Supporting Notes 1 and 4, and Table S1). Despite limited experimental data on nonstoichiometric compositions, we validated our methodology by benchmarking against known amorphous endmembers, namely, amorphous tellurium (a-Te) and stoichiometric amorphous tellurium dioxide (a-TeO₂), shown in Figure 1b. Structural analysis was performed using pair correlation functions, g(r), and effective coordination number (ECN), as detailed in the Supporting Note 2.

The pair correlation functions, in Figure 2a–c and Supporting Figure S2, exhibit a flattened profile beyond 6 Å, indicative of the absence of medium- and long-range order, confirming successful amorphisation. Our simulations accurately reproduce the pair correlation

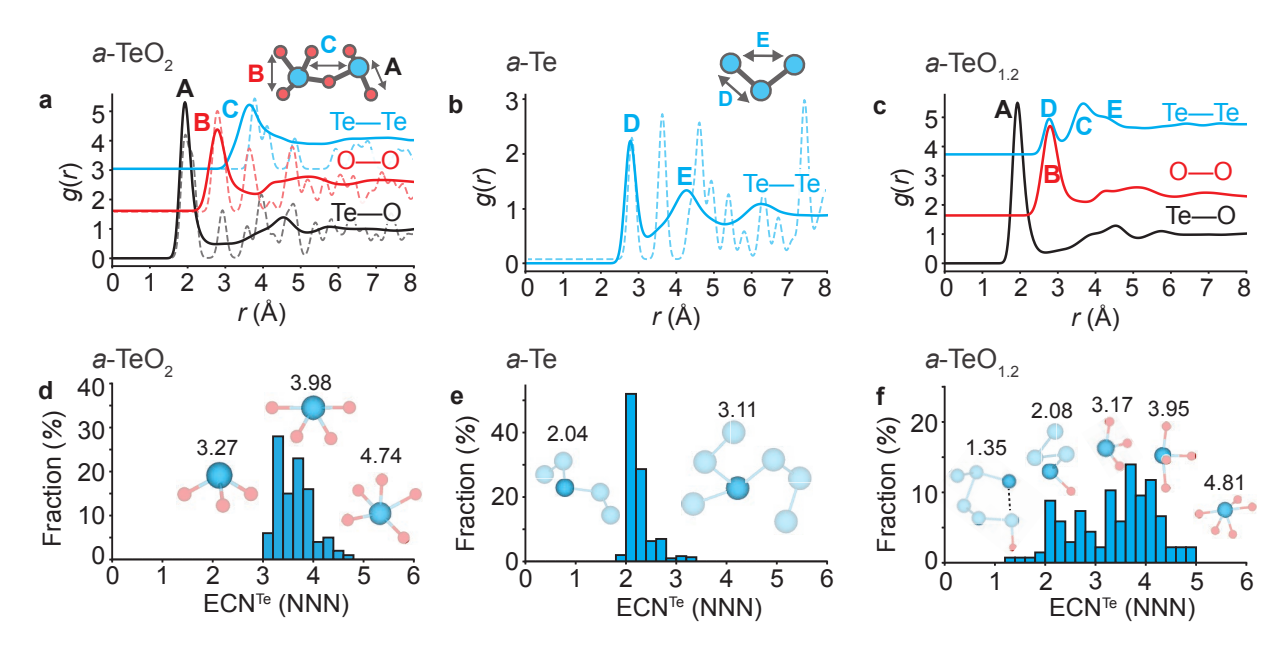


Figure 2: Pair correlation functions and distributions of tellurium coordination numbers. (a-c) Pair correlation functions, g(r), of (a) a-TeO₂, (b) a-Te, and (c) a-TeO_{1.2}; Radial atomic distributions of Te–O, O–O, and Te–Te pairs for the amorphous samples are displayed in solid lines; those for crystalline α -TeO₂ (paratellurite) and Te (trigonal) are shown in dashed lines. The peaks are labeled and assigned to atomic pairs of the structural fragments shown in the insets. The curves are shifted vertically for clarity. (d–f) Histograms of tellurium effective coordination number, ECN^{Te}, in number of nearest neighbors (NNN). The insets show fragments of the amorphous structures with corresponding ECN^{Te}.

peaks (Figure 2a,b) and coordination statistics (Figure 2d,e) reported for both a-TeO₂¹⁷ and a-Te, ²¹ with most experimental peak positions matched to within 0.03 Å. The average Te coordination numbers, n_{Te} , of 3.63 and 2.26 number of nearest neighbors (NNN) in a-TeO₂ and a-Te, respectively, are also consistent with reported values ^{17,21} (Supporting Table S4). This quantitative agreement across both extreme compositions, discussed in detail in the Supporting Note 3, provides support for the accuracy of the intermediate oxygen-poor models used in the subsequent analysis.

Thus, we turn to the structural results for the oxygen-deficient model with x = 1.2, the experimentally reported composition. ¹⁰ In addition to the features associated with TeO₂ glasses (peaks **A**, **B**, and **C**), the pair correlation function of a-TeO_{1.2} (Figure 2c) reveals two additional peaks. The first Te-Te pair peak, at 2.77 Å, aligns with peak **D** in a-Te, which has been observed in Fourier-transformed EXAFS spectra of Se-alloyed a-TeO_{1.2} samples. ¹⁰

The second peak, at 4.28 Å, also aligns with peak \mathbf{E} in a-Te and indicates the formation of extended Te chains. Along with the broad distribution of ECN^{Te} and representative structural motifs shown in Figure 2f, which cover coordination environments found in both a-Te and a-TeO₂, indicate the coexistence of two amorphous domains. While the hypothesis of the oxygen-deficient films being composed of biphasic Te-TeO_x mixture was raised by Liu et~al., ¹⁰ their atomistic model favors a picture of randomly dispersed oxygen vacancies stabilized by Te-Te bonds. This discrepancy justify closer examination, as detailed below.

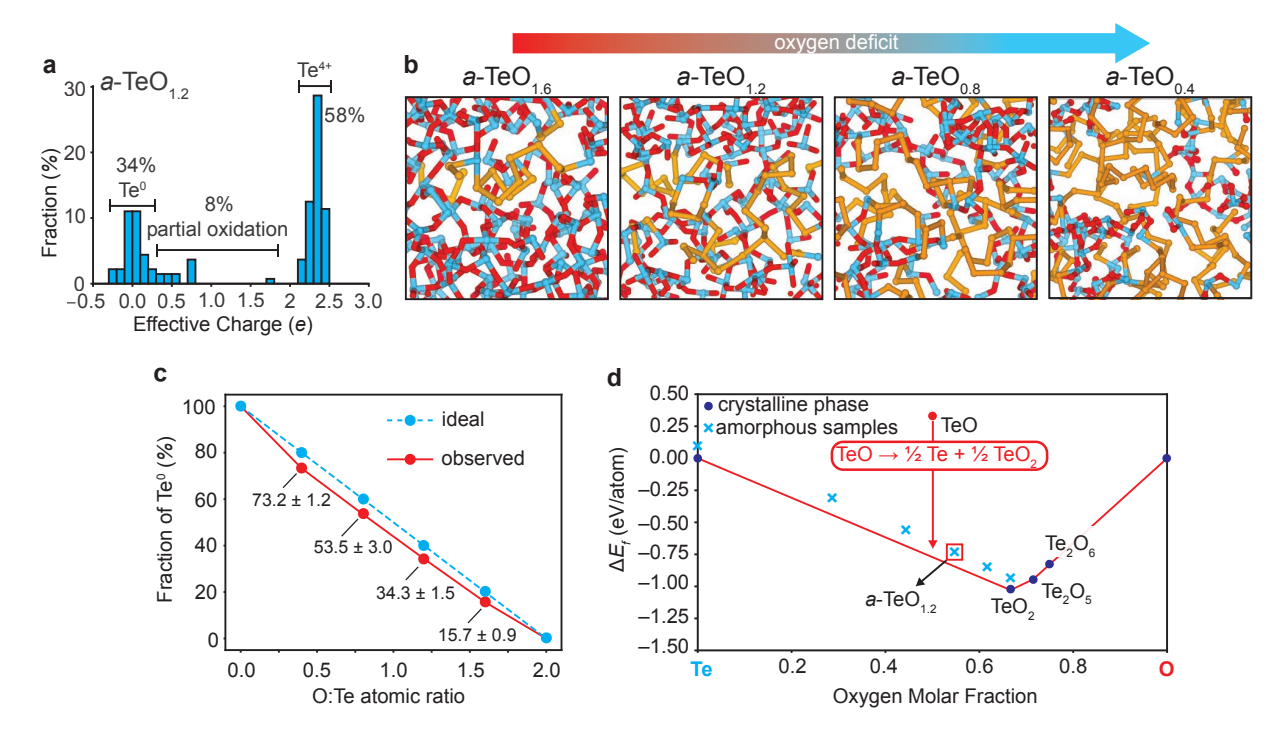


Figure 3: Structural and thermodynamic signatures of Te segregation in oxygen-deficient amorphous tellurium oxides. (a) Distribution of effective charges defined from the Bader analysis for a-TeO_{1.2} reveals three distinct populations of tellurium: neutral Te⁰ (34%), partially oxidized Te^{δ +} (8%), and fully oxidized Te^{δ +} (58%). Refer to the main text and Methods for further details on the classification criteria. (b) Structural snapshots of amorphous TeO_x for x = 1.6, 1.2, 0.8, and 0.4 reveal the progressive formation of a-Te domains (orange) as oxygen content decreases. (c) Fraction of Te⁰ extracted from Bader charge analysis compared to the ideal segregation model based on the composition (O:Te atomic ratio). (d) Formation energy convex hull for the Te-O binary system. Navy circles represent known crystalline phases on the convex hull, while blue crosses correspond to the simulated amorphous compositions. The elevated energy of a hypothetical hexagonal TeO structure (red circle), sourced from the Materials Project Database, ²⁹ illustrates the thermodynamic driving force for a-Te segregation in oxygen-deficient TeO_x.

To establish whether the phase separation inferred for x=1.2 ($a\text{-TeO}_{1.2}$) is a general feature of oxygen-deficient tellurium oxides, we extended our AIMD sampling to three more compositions, x=0.4, 0.8, and 1.6. We used a simple yet reliable metric derived from Bader analysis to quantify the fraction of each phase. Specifically, each tellurium atom is classified by its Bader charge into three populations (Figure 3a), neutral Te⁰ in the a-Te-like network, fully oxidized Te⁴⁺ characteristic of $a\text{-TeO}_2$, and a minor fraction of partially oxidized Te at the interfaces (see Methods for details). Our simulations reveal that a distinct a-Te network is already detectable at x=1.6, consistent with signs of direct Te-Te bonds reported as early as x=1.9. As shown in Figure 3b, this network expands progressively as the oxygen content decreases, at the expense of the $a\text{-TeO}_2$ matrix. The measured neutral-Te fraction (Figure 3c) closely follows the linear relationship expected for complete segregation.

Small deviations from the ideal line are attributed to partially oxidized atoms in the phase boundary, whose relative abundance is over-represented in our finite simulation cell. This behavior is consistent with bulk thermodynamics, as the convex-hull for the Te-O binary (Figure 3c) shows no stable compound between Te and TeO₂. For example, the hypothetical TeO structure, sourced from the Materials Project Database, ²⁹ lies far above the hull and would spontaneously decompose into the two end members. More importantly, the formation energies of our amorphous models lie just $96-137 \,\mathrm{meV}$ atom⁻¹ above the hull (Supporting Table S5). This lies within the range of known thermodynamic metastability, ³⁰ and is compatible with the long-term operational stability recently reported for films at x = 1.2. ¹⁰ These low formation energies also suggest modest interfacial energies between a-Te and a-TeO₂ domains, enabling the formation of interconnected networks. Together, these results indicate that oxygen deficiency beyond the dilute-vacancy limit drives the amorphous system to segregate into a-Te and a-TeO₂ domains, with only a thin interfacial region of partially oxidized Te.

Given that oxygen deficiency drives nanoscale segregation of a-Te and a-TeO₂, we now turn to its consequences for the electronic structure and, ultimately, for hole transport. Note

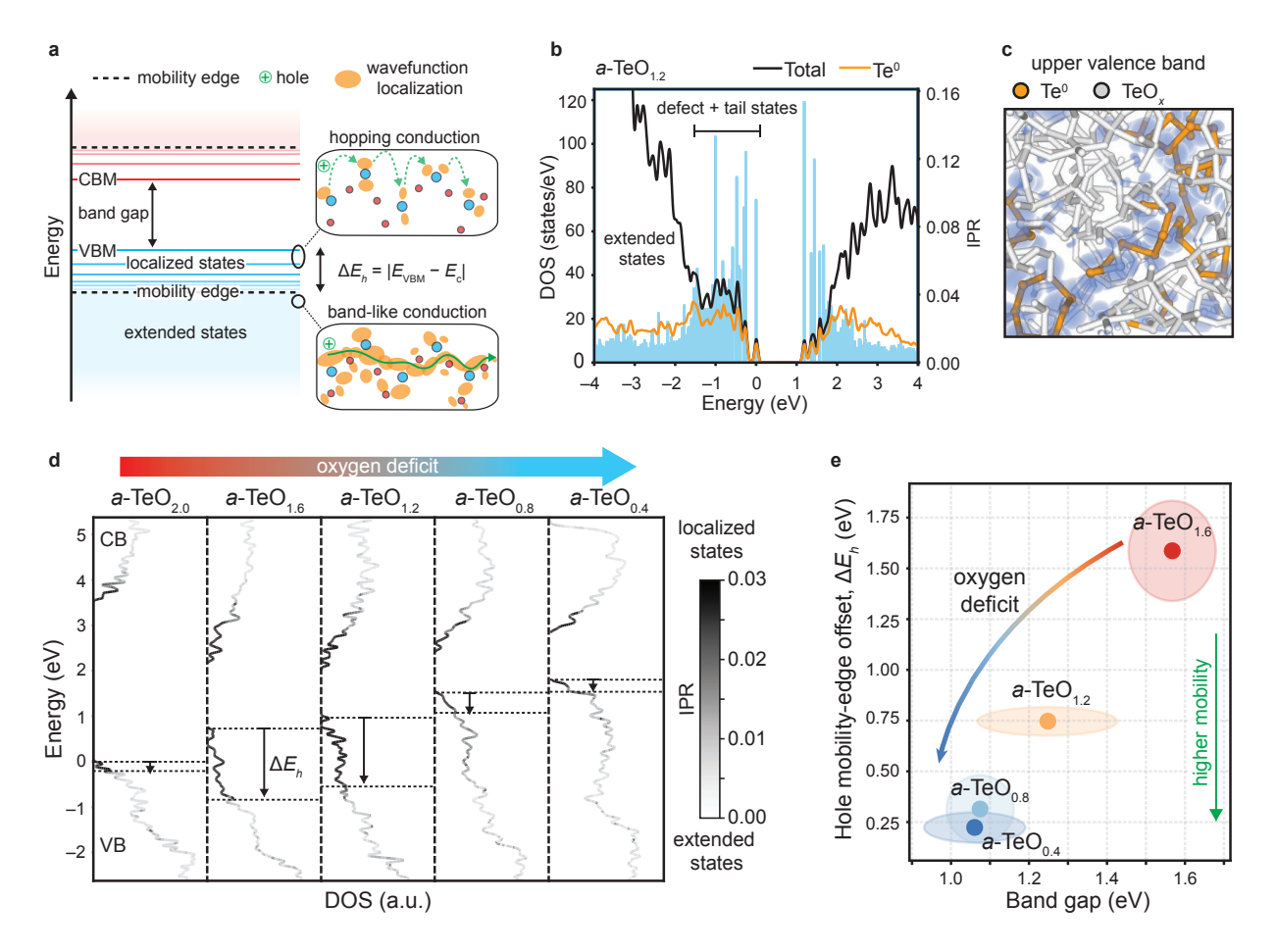


Figure 4: Electronic properties of oxygen-deficient amorphous TeO_x . (a) Schematic of hole conduction in an amorphous semiconductor. Spatial distribution of wavefunctions is depicted as orange clouds, while green arrows represent hole transport paths. The hole mobility-edge offset, defined as the energy difference between the VBM and the mobility edge ($\Delta E_h =$ $|E_{\text{VBM}}-E_c|$), represents the energetic barrier for accessing delocalized states and serves as an indicator of the potential for band-like hole transport. (b) Projected density of states (DOS) and inverse participation ratio (IPR, blue bars) for a-TeO_{1,2}, exhibiting localized states originated from Te⁰-rich regions nearby the band edges. (c) Spatial distribution of Te⁰ atoms (orange) within the TeO_x matrix (grey), illustrating the charge localization associated with the upper portion of the valence band. The isosurface corresponds to the states within 0.5 eV below the valence band maximum (VBM), plotted at an isovalue of 5% of the maximum charge density. (d) Evolution of the electronic structure across the a-TeO_x series (x = 2.0 to 0.4), with increasing oxygen deficiency. The DOS curves are aligned using the Te^{4+} 3d corelevel peak as a common energy reference, with the zero-energy level set to match the VBM of a-TeO₂. The grayscale color intensity reflects the degree of electronic localization within each energy interval, as indicated by the scale bar. (e) Hole mobility-edge offset, ΔE_h , versus band gap for different compositions, showing a strong correlation between oxygen deficiency and enhanced hole accessibility to extended states, with shaded ellipses indicating statistical variability across simulation samples.

that disorder broadens the band edges of amorphous oxides into a continuum of localized tail and defect states, ^{31,32} often blurring the definition of a band gap. ³³ Carrier transport typically occurs via thermally assisted hopping between localized states, until the carriers acquire sufficient energy to reach a critical threshold, Mott's mobility edge, ³¹ beyond which the electronic states become extended and band-like (Figure 4a). For holes, this mobility edge lies at a finite depth below the VBM, and identifying its position helps to rationalize the experimentally observed mobilities.

Figure 4b displays the projected density of states (DOS) for a-TeO_{1.2}, alongside the energy-resolved normalized inverse participation ratio (IPR), which quantifies spatial localization of the electronic states. As detailed in Methods, the normalized IPR tends toward zero for fully delocalized states and reaches unity for states entirely confined to a single atom. Again, our results contrast prior claims of shallow acceptor states in oxygen-poor samples 15 because the lowest unoccupied states lie near the conduction band, over 1 eV above the VBM, making thermal excitation unlikely. As anticipated from the schematic in Figure 4a, states at both band edges are strongly localized, with the IPR decreasing smoothly towards the band interior (see Figure 4b). More importantly, the upper valence band is dominated by the neutral Te atoms belonging to the a-Te network (Figure 4b,c), indicating that holes percolate through the pathways paved by these filaments. This result contrasts with that of Liu et al. 10 reporting, for the same composition (x = 1.2), an upper valence band delocalized across the entire supercell and strongly weighted by oxygen states. We attribute the discrepancy to methodological differences: specifically, their use of smaller cells (79 atoms), a quench rate approximately 33 times faster, likely trapping a melt-like configuration before phase separation could develop, and the PBE functional, which tends to over-delocalized electronic states.³⁴

Although there is no rigorous IPR threshold separating localized from extended states, we find that states with IPR < 0.03 behave electronically delocalized (Figure S3a). Therefore, we define the energy at which this criterion is first met as the hole mobility edge, and use

the energy difference between the VBM and this edge, ΔE_h , as a practical descriptor of how far a hole must relax to access high-mobility, band-like transport (Figure 4a). Aligning the DOS for the compositions $x = 2 \rightarrow 0.4$ (Figure 4d) reveals two clear trends. First, the VBM rises monotonically as oxygen content decreases, facilitating p-type doping. Second, among the oxygen-deficient samples, ΔE_h shrinks, making extended states increasingly accessible due to the improved connectivity of the a-Te sub-network (Figure S3b).

While lowering x may enhance hole transport, it also narrows the band gap from 3.51 eV at x=2 to $1.06\,\mathrm{eV}$ at x=0.4, gradually showing similar features to that of a-Te (Supporting Figure S4). Despite structural disorder and finite-size effects spreading the computed gaps in our simulation models ($\sigma\leqslant\pm0.18\,\mathrm{eV}$, Supporting Table 4), the averages align with experimental estimates of $3.76\,\mathrm{eV}$ for $a\text{-TeO}_2^{35}$ and $1.10\,\mathrm{eV}$ for $a\text{-TeO}_{1.2}^{10}$ thin films, supporting the reliability of the predicted band gap trends. The correlation between ΔE_h and the band gap, shown in Figure 4e, indicates that increases in hole mobility are accompanied by a reduction in the band gap, which is associated with increased off-state leakage and static power consumption in TFTs, consistent with reports from the original authors. ¹⁰ This effect, however, saturates below $x\sim1.2$, suggesting that reducing x to 0.4 may offer a viable route to improve hole transport without severely compromising device performance. Taken together, our results show that controlled oxygen content, via adjusting the oxygen partial pressure during vapor deposition ³⁶ or by co-evaporating elemental Te with TeO₂, provides a powerful, albeit antagonistic, handle to co-engineer the band gap and hole mobility in amorphous tellurium oxides.

X-ray absorption near-edge spectroscopy (XANES) of oxygen-deficient a-TeO_{1,2} thin films exhibits features of both TeO₂ and elemental Te, while Te 3d X-ray photoelectron spectra (XPS) confirms a metallic Te component. ¹⁰ Our atomistic simulations rationalize these findings by showing that oxygen loss leads to spontaneous phase segregation into interpenetrating networks of a-Te and a-TeO₂ (Figure 3b). As shown in Figure 3c, the quantitative estimate of neutral phase fractions was found to scale linearly with x, the O:Te atomic ratio. For

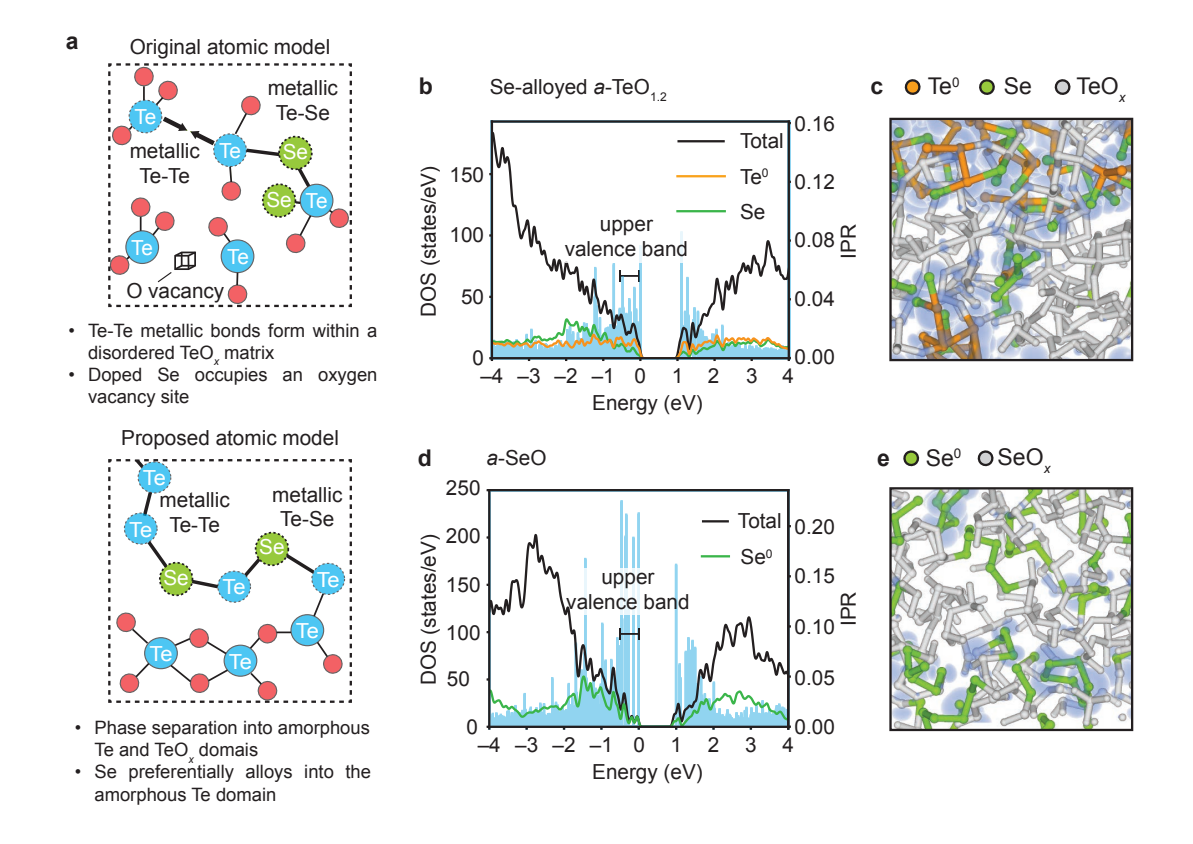


Figure 5: Electronic properties and atomic models of amorphous Se-alloyed $\text{TeO}_{1.2}$ and SeO_x . (a) Schematic comparison between the original (adapted from Liu $et.~al.^{10}$) and our proposed atomic models for Se-alloyed amorphous TeO_x . (b,d) Projected DOS and energy-resolved IPR of (b) Se-alloyed $a\text{-TeO}_{1.2}$ (Se_{0.33}TeO_{1.2}) and (d) a-SeO. (c,e) Spatial distribution of the upper valence band in (c) Se-alloyed $\text{TeO}_{1.2}$, showing the localization within the neutral Te^0 (orange) and Se (green) subnetwork, and in (e) a-SeO, highlighting the contribution from neutral Se atoms (green) within the oxidized matrix (grey). The isosurfaces in (c) and (e) are rendered using the same criteria as in Figure 4c.

x=1.2, our simulations predict 34% Te⁰, consistent with the 40% elemental Te inferred from bulk-sensitive XANES, ¹⁰ but significantly above the 9.7% metallic signal observed in surface-sensitive XPS, ¹⁰ likely due to under-sampling of the buried Te network. Furthermore, the electronic DOS coupled with IPR analysis (Figure 4b,d) reveals that the upper portion of the valence band is dominated by 5p orbitals of the neutral Te network, whereas extended states emerge only \sim 0.75 eV below the VBM. Consequently, we attribute the measured hole mobility of $4.2\,\mathrm{cm^2\,V^{-1}\,s^{-1}}$ to percolation-assisted hopping along the contiguous a-Te network, rather than to band-like transport, a hypothesis testable via temperature-dependent conductivity measurements. ³⁷

Concerning the origin of holes, our calculations confirm that oxygen vacancies remain deep donors (Figure 1e), and no low-lying unoccupied states are found across all compositions (Supporting Figure S4), ruling out the recently proposed oxygen-vacancy-induced "shallow acceptors" mechanism. ¹⁵ Instead, we evaluated tellurium vacancies as a potential hole source in oxygen-poor samples. These defects can form in both a-Te and a-TeO $_x$ domains (Figure S5a), with lower formation energies in the elemental domain due to weaker Te-Te bonds. Although Te vacancies have relatively low formation energies, down to $0.28\,\mathrm{eV}$, their appearance in our simulation cells remains unusual due to finite-size constraints. From Figure S5b,c, Te vacancies introduce shallow acceptor states near the VBM, supporting their role in enabling p-type conduction. An additional contribution may arise from hole injection at the interface with Ni contacts, consistent with the work-function offset between Ni $(5.15\,\mathrm{eV})$ and elemental Te $(4.95\,\mathrm{eV})$. ³⁸

In experiments, alloying the amorphous films with selenium significantly enhanced the TFT performance, increasing the hole mobility to $15 \,\mathrm{cm^2\,V^{-1}\,s^{-1}}$, and improving the on/off ratio from 10^4 to 10^7 . Thus, we extended our calculations to investigate the selenium doping effects in samples with the optimal composition (Se_{0.33}TeO_{1.2}), as described in the original study. Supporting Figure S6a reveals no Se–O bonding peak within 1.70 Å, with the first maximum only near 3.37 Å, while distinct signatures of direct SeTe and SeSe bonds are

present. Note that Se, like O and Te, belongs to group 16 and can exhibit both cationic and anionic behavior depending on its environment. Our simulations suggest that Se preferentially incorporates into the a-Te domain, forming a randomly mixed amorphous SeTe alloy. This contrasts with earlier models proposing Se substitution at oxygen vacancies within the oxide matrix (Figure 5a), and instead aligns with EXAFS evidence for SeTe metallic bonding. ¹⁰

As shown in Figure 5b, the VBM in the Se-alloyed sample consists of more delocalized states, as indicated by lower IPR values. Consequently, ΔE_h drops from 0.75 eV in the undoped oxide to 0.09 eV, as selenium enhances hole percolation not by bridging oxide fragments but by extending the conductive "highways" within the a-Te phase (Figure 5c). Incorporated into the a-Te domain, selenium behaves like tellurium, effectively mimicking the effect of relatively lower oxygen content, as $Se_{0.33}TeO_{1.2}$ exhibits connectivity comparable to a composition with x = 0.9, i.e., $(Se_{0.25}Te_{0.75})O_{0.9}$. These results contrast with recent findings suggesting that Se disrupts the Te network, ¹⁵ likely because those studies modeled substitutional rather than additive doping. Furthermore, our model indicates that higher levels of oxygen depletion, when combined with Se doping offer a path to mobilities above $15 \,\mathrm{cm}^2 \,\mathrm{V}^{-1} \,\mathrm{s}^{-1}$ without compromising off-state performance, potentially enabling faster switching speeds and broader applicability. Nevertheless, at very low x, the material approaches a-Te, which is known to recrystallize above $285 \,\mathrm{K}$, ³⁹ suggesting a potential stability limit to extreme oxygen deficiency.

Finally, the design principle of tuning hole transport via controlled oxygen deficiency and, by extension, phase segregation, may be generalized to other oxides. We demonstrate this by considering selenium dioxide (SeO₂), which, like TeO₂, lacks stable intermediary phases between elemental Se and SeO₂. Supporting Figure S6b displays evidence of elemental Se chains in the pair correlation function, indicating spontaneous biphasic separation. Thermodynamic analysis (Supporting Figure S7) places the amorphous sample 97 meV atom⁻¹ above the hull, comparable to the metastability of a-TeO_x. The hole states localize within neutral

Se domains (Figure 5d,e), but exhibit higher IPRs due to the more localized Se-4p orbitals, reflecting the increased hole effective mass of bulk Se $(1.4m_e)$ relative to Te $(0.2m_e)$. ⁴⁰ Overall, oxygen-deficient amorphous SeO_x displays analogous behavior to a-TeO_x, suggesting that this design principle can also enable a broader class of p-type amorphous semiconductors based on more earth-abundant elements.

Conclusions

We have reported a comprehensive theoretical investigation of oxygen-deficient amorphous tellurium oxides $(a\text{-TeO}_x)$ across a wide compositional range (x = 0.0, 0.4, 0.8, 1.2, 1.6, and)2.0), employing machine-learning-accelerated ab initio molecular dynamics and point-defect calculations. In contrast to previous models, our simulations revealed that oxygen removal does not lead to sparse vacancies, 10 nor "shallow acceptor states", 15 but rather to spontaneous phase segregation into continuous amorphous domains of neutral a-Te and insulating a-TeO₂, whose fractions scale linearly with the O:Te ratio. This two-phase picture unifies a suite of experimental observations: XANES and XPS signatures of elemental Te and EXAFS evidence for Te-Te (and Se-Te) metallic bonds. 10 Additionally, it helps to understand both the origin of holes and their transport mechanism. Holes are likely introduced by Te vacancies, or injected from Ni contacts into the Te-rich domains, given the lower work function of tellurium. In the oxygen-poor samples, the upper valence band is dominated by extended Te 5p states within the a-Te network, providing percolative "highways" for hole transport. The hole mobility, which depends on the connectivity of the neutral domain, scales with the concentration of the a-Te phase, establishing oxygen deficiency as a tunable parameter for optimizing p-type performance.

This new model explains the three-fold mobility boost (from 4.2 to $15 \,\mathrm{cm^2\,V^{-1}\,s^{-1}}$) achieved experimentally by Se doping. According to our calculations, Se atoms preferentially enter the a-Te domains rather than occupying the oxygen vacancy sites in the TeO_x

matrix, as previously suggested, 10 thereby extending the conductive network by mimicking higher oxygen deficiency. Therefore, mobilities exceeding current records can be attained at oxygen-poor compositions below x = 1.2 by concurrently incorporating dopants such as Se (to preserve off-state performance). The same concept of assisted percolation via neutral atomic domains may be generalizable to other amorphous oxides that (i) support a semiconducting elemental glass and (ii) lack intermediate crystalline compounds. Indeed, calculations on amorphous SeO_x confirmed analogous behavior, pointing to a broader materials design strategy for facilitating high-mobility p-type conduction in amorphous oxides, materials long constrained by poor hole transport.

Methods

DFT Calculations. First-principles calculations were performed within the framework of density functional theory (DFT) using the projector augmented wave ^{41,42} (PAW) method as implemented in the VASP code. ⁴³ Information on the PAW potentials is found within the Supporting Table S2. A cutoff energy of 520 eV was used for variable-volume calculations to reduce Pulay stress, while 400 eV was applied for constant-cell and static calculations. Lower cutoffs were sufficient for amorphous Te models: 227 eV during volume relaxation and 175 eV for subsequent steps. The Γ-point was sampled to integrate the Brillouin zone in all the calculations. To generate the amorphous models, AIMD simulations based on the meta-GGA r²SCAN functional²⁴ were done following a melt-and-quench protocol, summarized in Figure 1c. The AIMD trajectories were accelerated via the on-the-fly machine-learned force field (MLFF) framework available in VASP. ^{44–46} Refer to the Supporting Note 4 for on-the-fly training details and parameters. The amorphous structures were modeled in cubic supercells comprising 300 atoms, with a initial density of 5.6 g cm⁻³, which is close to experimental values reported for a-TeO_{1.2} ¹⁰ and a-TeO₂. ¹⁸ First, randomly-generated structures were pre-equilibrated under constant volume (NVT ensemble) at 2000 K for 2.5 ps (time step

5 fs), using the Langevin thermostat. ⁴⁸ A two-stage quenching (time step 1 fs) sequence followed: the systems were first quenched from 1500 K to 1200 K in the NVT ensemble over 10 ps, then cooled from 1200 K to 0 K in the NPT ensemble for 40 ps, corresponding to a cooling rate of $30\,\mathrm{K\,ps^{-1}}$. To prevent unphysical cell deformation at high temperatures, the supercells were constrained to maintain a cubic shape. The final structures were relaxed at 0 K using the r²SCAN functional, followed by an additional full relaxation with the HSE06^{3,4} hybrid functional to ensure accurate electronic structure characterization. For all geometry optimizations, energy and force convergence criteria were set to $1\times10^{-5}\,\mathrm{eV}$ and $0.03\,\mathrm{eV}\,\mathrm{\AA}^{-1}$, respectively.

Point-defect Calculations. For the α -TeO₂ point-defect calculations, we employed a 216-atom $3\times3\times2$ supercell and the same convergence criteria as in the amorphous simulations. Defect formation energies, E_f , were computed following established protocols, ^{13,49} defined for a defect D in charge state q as

$$E_f = \{ E[D^q] + E_{\text{corr}}[D^q] \} - E_P - \sum n_i \mu_i + q(\epsilon_{\text{VBM}} + \Delta \epsilon_F) , \qquad (1)$$

where $E[D^q]$ and E_P are the total energies of the defective and pristine supercells, respectively; n_i is the number of atoms of element i added $(n_i > 0)$ or removed $(n_i < 0)$; μ_i is the chemical potential of element i; ϵ_{VBM} is the VBM energy; and $\Delta \epsilon_F$ is the Fermi level relative to the VBM. The correction term $E_{\text{corr}}[D^q]$ accounts for finite-size effects under periodic boundary conditions and was evaluated using the extended FNV method. $^{49-51}$ To compute the dielectric profiles required for these corrections, the electronic contribution was obtained with HSE06, while the ionic part was calculated with PBEsol; for amorphous tellurium oxide, a 100-atom supercell was used for the ionic contribution due to computational costs. Defect modeling and parsing were performed with PYDEFECT. 52,53 Transition levels were defined as the Fermi-level positions at which the most stable charge state changes. Following defect convention, a defect is considered shallow if its transition level lies near a band edge,

facilitating ionization, and deep if it sits farther inside the band gap. For donor defects, such as O vacancies, we specifically examined transitions from neutral to positive charge states and their distance to the conduction band minimum. The atomic structures and isosurfaces were visualized using VESTA.⁵⁴

Bader Charges. The effective atomic charges were estimated as the difference between the number of valence electrons, Z_{val} , and the Bader charge, Q_{Bader} , namely, $Q_{\text{eff}} = Z_{\text{val}} - Q_{\text{Bader}}$. The Bader charges were computed by integrating the valence pseudocharge density within atomic compartments defined from the all-electron charge density, using the algorithm developed by Tang et al.⁵⁵ To identify atoms in the neutral state belonging to the a-Te domain, we classified Te atoms with effective Bader charges between -0.3 and +0.3e. Such small fluctuations are expected due to the way atomic volumes are partitioned in the Bader analysis and does not prejudice the distinction of reduced Te from oxidized species.

Inverse Participation Ratio. The inverse participation ratio (IPR) for each Kohn–Sham eigenstate was estimated using the projection of the atomic orbitals. Thus, the total weight of the atom i on the state n, $w_{i,n}$, was calculated by summing the squared modulus of projections over all angular momentum channels (ℓ, m) :

$$w_{i,n} = \sum_{\ell,m} |\langle \phi_{i,\ell m} | \psi_n \rangle|^2.$$
 (2)

The normalized IPR is then defined as:

$$IPR_{n} = \frac{\sum_{i} \left(\frac{w_{i,n}}{\sum_{j} w_{j,n}}\right)^{2} - \frac{1}{N}}{1 - \frac{1}{N}},$$
(3)

where N is the number of atoms in the system. This normalization ensures that $IPR_n = 0$ for a fully delocalized state and $IPR_n = 1$ for a state entirely localized on a single atom.

Supporting Information Available

The Supporting Information is available free of charge at https://pubs.acs.org/doi/xxx. Information on supporting data and methodological details underlying the main manuscript. Supporting Note 1 benchmarks various exchange–correlation functionals against structural and electronic properties of crystalline tellurium and tellurium oxides to justify the choice of r^2SCAN and HSE06. Supporting Note 2 describes the computation of pair correlation functions and effective coordination numbers used to characterize local atomic environments. Supporting Note 3 presents structural validation of a-Te and a-TeO₂, including comparison with experimental data. Supporting Note 4 outlines the computational setup and machine-learning parameters used in on-the-fly AIMD simulations. Finally, Supporting Note 5 provides additional thermodynamic, structural and electronic data across the a-TeO_x and Se-alloyed compositions, including thermodynamic stability, density of states, and radial distribution functions.

Competing interests

The authors declare no competing financial interests.

Acknowledgments

R.C.A. acknowledges the insightful comments from S. Jang (Tohoku University) on machine-learning force fields and molecular dynamics. This study was supported by JST FOREST Program (JPMJFR235S), KAKENHI (25K01486) and the E-IMR project at IMR, Tohoku University. Part of calculations were conducted using the facilities of the Supercomputer Center, the Institute for Solid State Physics, the University of Tokyo (Project ID: 2025-Ca-0135).

References

- (1) Medvedeva, J. E.; Buchholz, D. B.; Chang, R. P. H. Recent Advances in Understanding the Structure and Properties of Amorphous Oxide Semiconductors. Adv. Electron. Mater. 2017, 3, 1700082.
- (2) Kim, T.; Choi, C. H.; Hur, J. S.; Ha, D.; Kuh, B. J.; Kim, Y.; Cho, M. H.; Kim, S.; Jeong, J. K. Progress, Challenges, and Opportunities in Oxide Semiconductor Devices: A Key Building Block for Applications Ranging from Display Backplanes to 3D Integrated Semiconductor Chips. Adv. Mater. 2023, 35, 2204663.
- (3) Kamiya, T.; Hosono, H. Material Characteristics and Applications of Transparent Amorphous Oxide Semiconductors. NPG Asia Mater. 2010, 2, 15–22.
- (4) Zhu, Y.; He, Y.; Jiang, S.; Zhu, L.; Chen, C.; Wan, Q. Indium-gallium-zinc-oxide Thin-film Transistors: Materials, Devices, and Applications. J. Semicond. 2021, 42, 031101.
- (5) Mizuno, K.; Izaki, M.; Murase, K.; Shinagawa, T.; Chigane, M.; Inaba, M.; Tasaka, A.; Awakura, Y. Structural and Electrical Characterizations of Electrodeposited p-Type Semiconductor Cu₂O Films. J. Electrochem. Soc. 2005, 152, C179.
- (6) Kawazoe, H.; Yasukawa, M.; Hyodo, H.; Kurita, M.; Yanagi, H.; Hosono, H. p-type Electrical Conduction in Transparent Thin Films of CuAlO₂. *Nature* **1997**, *389*, 939–942.
- (7) Varley, J. B.; Schleife, A.; Janotti, A.; Van de Walle, C. G. Ambipolar doping in SnO. *Appl. Phys. Lett.* **2013**, *103*, 082118.
- (8) Hautier, G.; Miglio, A.; Ceder, G.; Rignanese, G.-M.; Gonze, X. Identification and Design Principles of Low Hole Effective Mass p-type Transparent Conducting Oxides. Nat. Commun. 2013, 4, 2292.

- (9) Schoop, L. M.; Müchler, L.; Felser, C.; Cava, R. J. Lone Pair Effect, Structural Distortions, and Potential for Superconductivity in Tl Perovskites. *Inorg. Chem.* **2013**, *52*, 5479–5483.
- (10) Liu, A.; Kim, Y.-S.; Kim, M. G.; Reo, Y.; Zou, T.; Choi, T.; Bai, S.; Zhu, H.; Noh, Y.-Y. Selenium-Alloyed Tellurium Oxide for Amorphous p-channel Transistors. *Nature* **2024**, 629, 798–802.
- (11) Costa-Amaral, R.; Bae, S.; Vu, T. N. H.; Kumagai, Y. Exploring Intrinsic and Extrinsic p-Type Dopability of Atomically Thin β-TeO₂ from First Principles. ACS Appl. Mater. Interfaces 2024, 17, 1605–1614.
- (12) Xiao, Z.; Qiu, C.; Wei, S.-H.; Hosono, H. Is p-Type Doping in TeO₂ Feasible? *Chin. Phys. Lett.* **2025**, *42*, 016103.
- (13) Freysoldt, C.; Grabowski, B.; Hickel, T.; Neugebauer, J.; Kresse, G.; Janotti, A.; Van de Walle, C. G. First-principles Calculations for Point Defects in Solids. Rev. Mod. Phys. 2014, 86, 253–305.
- (14) Oba, F.; Kumagai, Y. Design and Exploration of Semiconductors from First Principles: A Review of Recent Advances. *Appl. Phys. Express* **2018**, *11*, 060101.
- (15) Hao, K.-R.; Wang, X.; Bai, Z.; Deng, J.; Yan, Q.-B.; Wang, G.; Zhao, C. Effects of Defects and Dopants on p-type Selenium-doped Amorphous Tellurium Oxide: Electronic Structure and Transistor Performance from Multiscale Modeling. Phys. Rev. Appl. 2025, 23, 054072.
- (16) Hume-Rothery, W. VIII. The Crystal Structures of the Elements of the B Sub-groups and their Connexion with the Periodic Table and Atomic Structures. *Lond. Edinb. Dubl. Phil. Mag.* **1930**, *9*, 65–80.

- (17) Champness, C. H.; Kipling, A. L. Transport Measurements in Annealed Single Crystal Tellurium. Can. J. Phys. 1970, 48, 3038–3046.
- (18) Strand, J.; Shluger, A. L. On the Structure of Oxygen Deficient Amorphous Oxide Films. Adv. Sci. 2023, 11.
- (19) Pham, H. H.; Wang, L.-W. Oxygen Vacancy and Hole Conduction in Amorphous TiO₂.

 Phys. Chem. Chem. Phys. **2015**, 17, 541–550.
- (20) Deringer, V. L.; Stoffel, R. P.; Dronskowski, R. Thermochemical Ranking and Dynamic Stability of TeO₂ Polymorphs from Ab Initio Theory. Cryst. Growth Des. 2014, 14, 871–878.
- (21) Wang, W.; Janotti, A.; Van de Walle, C. G. Role of Oxygen Vacancies in Crystalline WO₃. J. Mater. Chem. C **2016**, 4, 6641–6648.
- (22) Buckeridge, J.; Catlow, C. R. A.; Farrow, M. R.; Logsdail, A. J.; Scanlon, D. O.; Keal, T. W.; Sherwood, P.; Woodley, S. M.; Sokol, A. A.; Walsh, A. Deep vs Shallow Nature of Oxygen Vacancies and Consequent n-type Carrier Concentrations in Transparent Conducting Oxides. *Phys. Rev. Mater.* 2018, 2, 054604.
- (23) Kudo, S.; Yamasaki, T.; Suzuki, I.; Dorai, A.; Costa-Amaral, R.; Bae, S.; Kumagai, Y.; Tanimura, H.; Ichitsubo, T.; Omata, T. Role of Hydrogen in the n-type Oxide Semiconductor MgIn₂O₄: Experimental Observation of Electrical Conductivity and First-principles Insight. *APL Materials* **2025**, *13*, 041118.
- (24) Furness, J. W.; Kaplan, A. D.; Ning, J.; Perdew, J. P.; Sun, J. Accurate and Numerically Efficient r²SCAN Meta-Generalized Gradient Approximation. J. Phys. Chem. Lett. 2020, 11, 8208–8215.
- (3) Heyd, J.; Scuseria, G. E.; Ernzerhof, M. Hybrid Functionals Based on a Screened Coulomb Potential. J. Chem. Phys. 2003, 118, 8207–8215.

- (4) Krukau, A. V.; Vydrov, O. A.; Izmaylov, A. F.; Scuseria, G. E. Influence of the Exchange Screening Parameter on the Performance of Screened Hybrid Functionals. J. Chem. Phys. 2006, 125, 224106.
- (17) Alderman, O. L. G.; Benmore, C. J.; Feller, S.; Kamitsos, E. I.; Simandiras, E. D.; Liakos, D. G.; Jesuit, M.; Boyd, M.; Packard, M.; Weber, R. Short-Range Disorder in TeO₂ Melt and Glass. J. Phys. Chem. Lett. 2019, 11, 427–431.
- (21) Ichikawa, T. Electron Diffraction Study of the Local Atomic Arrangement in Amorphous Tellurium Films. *Phys. Status Solidi B* **1973**, *56*, 707–715.
- (29) Jain, A.; Ong, S. P.; Hautier, G.; Chen, W.; Richards, W. D.; Dacek, S.; Cholia, S.; Gunter, D.; Skinner, D.; Ceder, G.; Persson, K. A. Commentary: The Materials Project: A Materials Genome Approach to Accelerating Materials Innovation. APL Materials 2013, 1, 011002.
- (30) Sun, W.; Dacek, S. T.; Ong, S. P.; Hautier, G.; Jain, A.; Richards, W. D.; Gamst, A. C.; Persson, K. A.; Ceder, G. The Thermodynamic Scale of Inorganic Crystalline Metastability. Sci. Adv. 2016, 2, e1600225.
- (31) Mott, N. The Mobility Edge Since 1967. *J. Phys. C: Solid State Phys.* **1987**, *20*, 3075–3102.
- (32) Pan, Y.; Inam, F.; Zhang, M.; Drabold, D. A. Atomistic Origin of Urbach Tails in Amorphous Silicon. *Phys. Rev. Lett.* **2008**, *100*, 206403.
- (33) de Jamblinne de Meux, A.; Pourtois, G.; Genoe, J.; Heremans, P. Comparison of the Electronic Structure of Amorphous versus Crystalline Indium Gallium Zinc Oxide Semiconductor: Structure, Tail States and Strain Effects. J. Phys. D: Appl. Phys. 2015, 48, 435104.

- (34) Cohen, A. J.; Mori-Sńchez, P.; Yang, W. Insights into Current Limitations of Density Functional Theory. *Science* **2008**, *321*, 792–794.
- (35) Nayak, R.; Gupta, V.; Dawar, A.; Sreenivas, K. Optical Waveguiding in Amorphous Tellurium Oxide Thin Films. *Thin Solid Films* **2003**, *445*, 118–126.
- (36) Ogbuu, O.; Du, Q.; Lin, H.; Li, L.; Zou, Y.; Koontz, E.; Smith, C.; Danto, S.; Richardson, K.; Hu, J. Impact of Stoichiometry on Structural and Optical Properties of Sputter Deposited Multicomponent Tellurite Glass Films. J. Am. Ceram. Soc. 2015, 98, 1731–1738.
- (37) Mott, N. F. Conduction in Non-crystalline Materials: III. Localized States in a Pseudogap and Near Extremities of Conduction and Valence Bands. *Philos. Mag.* 1969, 19, 835–852.
- (38) Michaelson, H. B. The Work Function of the Elements and its Periodicity. *J. Appl. Phys.* **1977**, 48, 4729–4733.
- (39) Blum, N. A.; Feldman, C. Mössbauer Study of Amorphous and Crystalline Tellurium. Solid State Commun. 1974, 15, 965–968.
- (40) Beyer, W.; Mell, H.; Stuke, J. Conductivity and Thermoelectric Power of Trigonal Se_xTe_{1-x} Single Crystals. *Phys. Status Solidi B* **1971**, 45, 153–162.
- (41) Blöchl, P. E. Projector Augmented-Wave Method. *Phys. Rev. B* **1994**, *50*, 17953–17979.
- (42) Kresse, G.; Joubert, D. From Ultrasoft Pseudopotentials to the Projector Agumented-Wave Method. *Phys. Rev. B* **1999**, *59*, 1758–1775.
- (43) Kresse, G.; Hafner, J. Ab Initio Molecular Dynamics for Open-Shell Transition Metals. *Phys. Rev. B* **1993**, *48*, 13115–13118.
- (44) Jinnouchi, R.; Karsai, F.; Kresse, G. On-the-fly Machine Learning Force Field Generation: Application to Melting Points. *Phys. Rev. B* **2019**, *100*, 014105.

- (45) Jinnouchi, R.; Lahnsteiner, J.; Karsai, F.; Kresse, G.; Bokdam, M. Phase Transitions of Hybrid Perovskites Simulated by Machine-Learning Force Fields Trained on the Fly with Bayesian Inference. *Phys. Rev. Lett.* **2019**, *122*, 225701.
- (46) Jinnouchi, R.; Karsai, F.; Verdi, C.; Asahi, R.; Kresse, G. Descriptors Representing Two- and Three-body Atomic Distributions and Their Effects on the Accuracy of Machine-learned Inter-atomic Potentials. J. Chem. Phys. 2020, 152, 234102.
- (18) Gulenko, A.; Masson, O.; Berghout, A.; Hamani, D.; Thomas, P. Atomistic Simulations of TeO₂-based Glasses: Interatomic Potentials and Molecular Dynamics. *Phys. Chem. Chem. Phys.* **2014**, *16*, 14150–14160.
- (48) Hoover, W. G.; Ladd, A. J. C.; Moran, B. High-Strain-Rate Plastic Flow Studied via Nonequilibrium Molecular Dynamics. *Phys. Rev. Lett.* **1982**, *48*, 1818–1820.
- (49) Kumagai, Y.; Oba, F. Electrostatics-based Finite-size Corrections for First-principles Point Defect Calculations. *Phys. Rev. B* **2014**, *89*, 195205.
- (50) Freysoldt, C.; Neugebauer, J.; Van de Walle, C. G. Fully Ab Initio Finite-Size Corrections for Charged-Defect Supercell Calculations. *Phys. Rev. Lett.* **2009**, *102*, 016402.
- (51) Kumagai, Y.; Choi, M.; Nose, Y.; Oba, F. First-principles Study of Point Defects in Chalcopyrite ZnSnP₂. Phys. Rev. B **2014**, 90, 125202.
- (52) Kumagai, Y. PYDEFECT. Available at https://kumagai-group.github.io/pydefect, accessed on January 24, 2025.
- (53) Kumagai, Y.; Tsunoda, N.; Takahashi, A.; Oba, F. Insights into Oxygen Vacancies from High-throughput First-principles Calculations. *Phys. Rev. Mater.* **2021**, *5*, 123803.
- (54) Momma, K.; Izumi, F. VESTA 3 for Three-dimensional Visualization of Crystal, Volumetric and Morphology Data. *J. Appl. Cryst.* **2011**, *44*, 1272–1276.

(55) Tang, W.; Sanville, E.; Henkelman, G. A Grid-based Bader Analysis Algorithm without Lattice Bias. *J. Phys.: Condens. Matter* **2009**, *21*, 084204.

Supporting Information:

Atomic networks as highways for holes in oxygen-deficient amorphous oxides

Supporting Note 1: Benchmark of exchange-correlation functionals

Owing to the known sensitivity of Te-based glasses to the choice of exchange–correlation functional, 1,2 we benchmarked GGA, meta-GGA, and hybrid functionals against the structural and electronic properties of c-Te, α -, β -, and γ -TeO₂, and Te₂O₅, as summarized in Table S1. While these crystalline phases differ from the amorphous state, they offer a computationally affordable basis for assessing functional performance across relevant local bonding environments. Except for trigonal Te, best described by PBE, the meta-GGA r²SCAN functional achieved the best balance of accuracy and cost and was therefore adopted for quenching simulations. The HSE06 hybrid functional 3,4 was used post-quench to relaxed the volume and atomic positions, while refining the electronic structure.

Table S1: Calculated lattice parameters (a,b,c in Å), cell volume V (Å³) and band gap, E_g (eV), for trigonal Te (c-Te) and Te–O compounds. Percent errors with respect to experiment are given in parentheses.

Crystal	Functional	a (Å)	b (Å)	c (Å)	V (Å ³)	$E_g \text{ (eV)}$
c-Te		<u>`</u>		· · ·	· · · · · · · · · · · · · · · · · · ·	<u> </u>
	PBE	4.51 (1.16)	4.51 (1.16)	5.96 (0.70)	104.92 (3.05)	0.17(-48.12)
	PBEsol	$4.31 \ (-3.28)$	$4.31 \ (-3.28)$	5.96(0.73)	$95.94 \ (-5.77)$	0 (metal)
	$\rm r^2SCAN$	4.60(3.19)	4.60(3.19)	5.92(-0.05)	108.36 (6.43)	0.47(47.50)
	HSE06	4.62(3.64)	4.62(3.64)	5.80(-2.03)	107.14(5.23)	0.89 (177.19)
	$\mathrm{Exp.}^{5}$	4.46	4.46	5.92	101.81	0.32^{6}
α -TeO ₂						
	PBE	4.98(3.43)	4.98(3.43)	7.62(0.12)	188.84 (7.10)	2.80 (-20.03)
	PBEsol	4.82(0.21)	4.82(0.21)	7.44(-2.26)	173.06 (-1.85)	2.83 (-19.14)
	r^2SCAN	4.84 (0.47)	4.84 (0.47)	7.67(0.70)	$179.25 \ (1.65)$	3.41 (-2.60)
	HSE06	4.87(1.12)	4.87(1.12)	7.65 (0.42)	181.04 (2.67)	4.15 (18.43)
	$\mathrm{Exp.}^{7}$	4.81	4.81	7.62	176.33	3.50^{8}
β -TeO ₂						
	PBE	5.59(2.30)	5.75(2.58)	$12.33\ (2.43)$	$396.39\ (7.51)$	2.25 (-39.24)
	PBEsol	5.33(-2.49)	5.70(1.66)	11.85 (-1.52)	360.02 (-2.36)	2.02 (-45.43)
	r^2SCAN	5.44 (-0.37)	5.63(0.32)	$12.33\ (2.46)$	377.57(2.40)	2.76 (-25.49)
	HSE06	5.52 (0.95)	5.62(0.17)	12.49(3.81)	387.03 (4.97)	3.64 (-1.68)
	$\mathrm{Exp.}^9$	5.46	5.61	12.04	368.71	3.70^{10}
γ -TeO ₂						
	PBE	4.48(2.99)	5.11(4.35)	8.81(2.75)	$201.82\ (10.42)$	3.05 (-10.50)
	PBEsol	4.27 (-1.98)	$4.93 \ (0.67)$	8.53 (-0.49)	179.46 (-1.81)	3.08 (-9.77)
	r^2SCAN	$4.41 \ (1.41)$	4.87 (-0.51)	8.75 (1.99)	188.07 (2.90)	3.63 (6.36)
	HSE06	4.47(2.63)	4.93 (0.59)	$8.82\ (2.82)$	193.98 (6.14)	4.37 (28.09)
	Exp. ¹¹	4.35	4.90	8.58	182.77	3.41^{12}
${ m Te_2O_5}$						
	PBE	5.51(2.71)	4.80(2.21)	8.16(2.61)	210.85 (8.77)	1.68
	PBEsol	5.46(1.77)	4.71 (0.38)	$8.00 \ (0.53)$	200.49(3.42)	1.82
	r^2SCAN	$5.40 \ (0.63)$	4.72(0.53)	$8.00 \ (0.53)$	197.79(2.02)	2.39
	HSE06	5.39(0.45)	4.74 (0.92)	8.06 (1.27)	200.66 (3.50)	3.05
	Exp. ¹³	5.37	4.70	7.96	193.86	_

Supporting Note 2: Assessment of structural order and local atomic environments

To assess structural order in our amorphous models, we used the pair-correlation (radial distribution) function, $g_{AB}(r)$, or just g(r), which quantifies the probability of finding a particle of type B at a distance r from a particle of type A, relative to an ideal gas with density ρ_B . The $g_{AB}(r)$ function is computed as:

$$g_{AB}(r) = \frac{1}{4\pi r^2 \rho_B N_A \Delta r} \sum_{i \in A} \sum_{j \in B} \Theta\left(r + \frac{\Delta r}{2} - r_{ij}\right) \Theta\left(r_{ij} - \left(r - \frac{\Delta r}{2}\right)\right), \quad (S1)$$

where N_A is the number of A atoms, r_{ij} the interatomic distance, Δr the histogram bin width, and Θ the Heaviside step function selecting pairs within the shell centered at r. Complementarily, to describe local atomic environments in disordered systems, we used the effective coordination number (ECN), 14,15 which is particularly suitable for amorphous materials, where bond lengths vary significantly. The ECN assigns a continuous weight to each bond rather than relying on a fixed cutoff, for an atom i it is defined as:

$$ECN_i = \sum_{j} \exp\left[1 - \left(\frac{d_{ij}}{d_{av}^i}\right)^6\right],\tag{S2}$$

where d_{ij} is the distance between atoms i and j, and d_{av}^i is the atom-specific average bond length computed self-consistently via: ¹⁶

$$d_{\text{av}}^{i} = \frac{\sum_{j} d_{ij} \exp\left[1 - \left(\frac{d_{ij}}{d_{av}^{i}}\right)^{6}\right]}{\sum_{j} \exp\left[1 - \left(\frac{d_{ij}}{d_{av}^{i}}\right)^{6}\right]}.$$
 (S3)

The iteration begins with the shortest bond length from atom i, and converges when the change in d_{av}^i between successive steps is smaller than 1×10^{-4} Å. This formulation allows for a smooth distinction between strong and weak bonding contributions, enabling consistent

coordination analysis in both ordered and disordered systems.

Supporting Note 3: Structural features of amorphous Te and TeO_2

Fig. 2 of the main manuscript summarizes the structural characteristics of the amorphous models, presenting pair correlation functions with each peak assigned to its bonding environment, and histograms of the tellurium effective coordination numbers, ECN^{Te}; the corresponding g(r) peak positions and the average tellurium ECN, n_{Te} , in number of nearest neighbors (NNN) are compiled in Table S4. In a-TeO₂, peak A (1.94 Å) corresponds to the Te-O bond, while peaks B (2.79 Å) and C (3.66 Å) arise from intra-unit O-O and inter-unit Te-Te distances, respectively. These peak positions closely match experimental values of 1.93 Å, 2.79 Å, and 3.55 Å from high-resolution X-ray pair distribution functions of TeO₂ glasses ¹⁷ (Table S4). The ECN^{Te} distribution (Fig. 2d) reveals three- to five-fold coordination environments, consistent with prior theoretical models.^{2,18} The computed average of 3.63 NNN falls slightly below the experimental value of 4.0, ¹⁷ but lies within the reported range of 3.6-4.0, $^{2,18-20}$ reflecting the inherent ambiguity in defining Te-O cutoffs in disordered networks. In a-Te, peaks \mathbf{D} (2.79 Å) and \mathbf{E} (4.27 Å) correspond to the first and second Te-Te neighbors within chain-like motifs, in agreement with electron diffraction data. ²¹ A minor population of threefold coordinated Te atoms (Fig. 2e) yields an average coordination number of 2.26 NNN, consistent with prior ab initio molecular dynamics estimates (2.12-2.69). This strong agreement across both stoichiometric endmembers supports the fidelity of our methodology in capturing the local environments of intermediate oxygen-deficient phases.

Supporting Note 4: Computational Details and Machine Learning Parameters

The projector augmented wave (PAW) potentials used in this study are listed in Table S2. We initially attempted to run the molecular dynamics entirely using machine-learning force fields (MLFFs). However, this led to unphysical dynamics, structural collapse, or divergent cell volumes, likely due to the need for a much larger sampling space and longer training times, given the disordered nature of the structures. Additionally, the presence of multiple compositions introduced challenges in transferring the MLFFs across different O:Te ratios. We therefore switched to on-the-fly learning, triggering *ab initio* evaluations whenever the predicted error exceeded a threshold. Each quenching process was divided into five independent and sequential runs of 10 ps, with no force field pretraining or transfer between runs. While a higher number of *ab initio* evaluations was performed, this approach yielded stable trajectories across all compositions without relying on transferable MLFFs, ensuring simulations consistent with experiments, as discussed in Supporting Note 3. The VASP machine-learning parameters are summarized in Table S3.

Table S2: Information on the PAW data sets adopted in this study.

Element	VASP symbol	Valence orbitals
О	O	$(2s)^2 (2p)^4$
Te	Te	$(5p)^4 (5s)^2$
Se	Se	$(4s)^2 (4p)^4$

Table S3: Machine-learning INCAR parameters used for on-the-fly accelerated *ab initio* molecular dynamics.

Flag	Value used
ML_LMLFF	.TRUE.
ML_MODE	train
$ML_{-}ISTART$	0
ML_RCUT1	8.0
ML_SION1	0.5
ML_MRB1	12
ML_DESC_TYPE	0
ML_RCUT2	5.0
ML_SION2	0.5
ML_MRB2	8
ML_LMAX2	3
$\mathtt{ML_ICRITERIA}$	1
ML_IUPDATE_CRITERIA	1
$\mathtt{ML_CTIFOR}$	0.002
ML_SCLC_CTIFOR	0.6
ML_CX	0

Supporting Note 5: Extra structural and electronic data

This section provides additional structural and electronic details of the amorphous TeO_x and Se-alloyed samples discussed in the main text. Figure S1 shows the relative stability of oxygen vacancies in three different sites of amorphous TeO_x , the lowest energy one was considered for the charge defect analysis. Table S4 summarizes the peaks positions in the pair-correlation functions, g(r), and average effective coordination number of Te for the amorphous structures, obtained from simulations and experiments. Table S5 contains the formation energies relative to the convex hull, E_{hull} , band gaps, and hole mobility edge offsets, ΔE_h , for representative samples, supporting their thermodynamic metastability and tunable transport characteristics. Figure S2 shows the pair-correlation functions, g(r), for Te-Te, Te-O, and O-O pairs across all compositions, confirming structural consistency and reproducibility across samples. The corresponding total and projected density of states (DOS) are shown in Figure S4, where contributions from neutral Te⁰ highlight their role

in shaping the upper valence band. In Figure S3, we show the spacial distribution of the individual eigenstates and the associated inverse participation ratio (IPR), trends in the localization of the upper valance band along the compositional series of the amorphous structures are also displayed. The energetics of Te vacancies are shown in Figure S5, together with DOS evidence of their acceptor-like nature. Figure S6 extends the structural analysis to Se-alloyed a-TeO_{1.2} and amorphous SeO_x, reinforcing the reproducibility and revealing differences in bonding environments. Finally, the thermodynamic stability of amorphous SeO_x is evaluated in Figure S7, which places the composition within a similar metastability range as the tellurium-based counterparts.

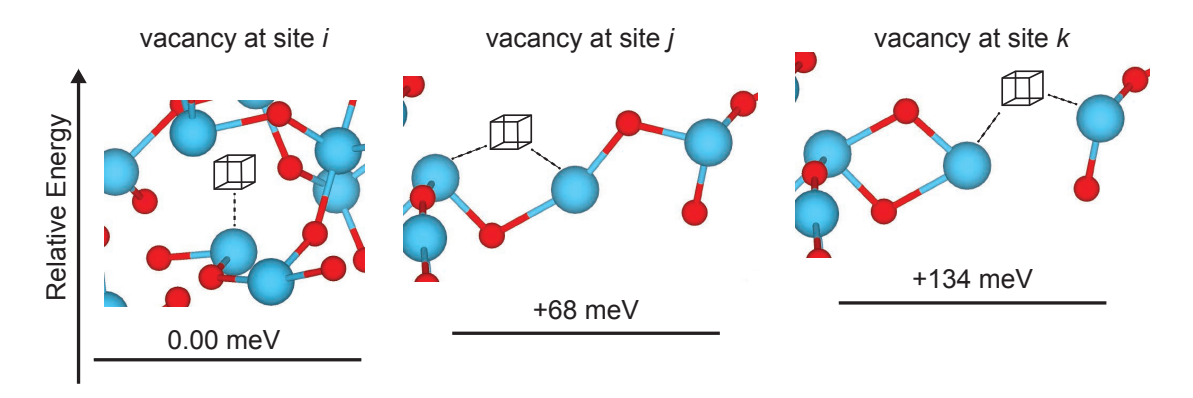


Figure S1: Local atomic environments for three distinct vacancy sites (i-k), with relative energies of 0.00, +68, and +134 meV per vacancy, respectively. Vacancies are indicated by transparent cubes, whereas Te and O atoms are shown in blue and red.

Table S4: Pair-correlation function, g(r), peak positions (in Å) and average effective coordination number of Te (n_{Te}) for the investigated structures, compared to experimental data.

		g(r) peaks					
		A	В	С	D	\mathbf{E}	n_{Te}
a-TeO ₂	This work	1.94	2.79	3.66	_	_	3.63
a-1eO ₂	$\mathrm{Exp.}^{17}$	1.93	2.79	3.55	_	_	4
$a ext{-TeO}_{1.2}$	This work	1.94	2.80	3.67	2.77	4.28	3.05
a-Te	This work	_	_	_	2.79	4.27	2.19
<i>a</i> -1e	$\mathrm{Exp.}^{21}$	_	_	_	2.80	4.25	1.8

Table S5: Formation energies relative to the convex hull, $E_{\rm hull}$ (meV/atom), band gap, E_g (eV), and hole mobility edge offsets, ΔE_h (eV), for representative amorphous ${\rm TeO}_x$ samples and Se-alloyed $a{\text -}{\rm TeO}_{1.2}$.

Composition	Sample	$E_{\rm hull}~({\rm meV/atom})$	$E_g \text{ (eV)}$	$\Delta E_h \text{ (eV)}$
a -TeO $_{0.4}$				
	1	145.87	1.06	0.30
	2	134.74	1.22	0.12
	3	129.16	0.90	0.25
	Average	136.59	1.06	0.22
a- TeO _{0.8}				
	1	137.33	1.19	0.41
	2	139.99	1.06	0.08
	3	121.52	0.98	0.45
	Average	132.95	1.07	0.31
a-TeO _{1.2}				
	1	115.72	1.06	0.75
	2	120.24	1.19	0.66
	3	108.38	1.49	0.83
	Average	114.78	1.25	0.75
a-TeO _{1.6}				
	1	114.20	1.68	1.56
	2	117.34	1.60	1.30
	3	99.96	1.42	1.90
	Average	110.50	1.57	1.59
Se-alloyed				
	1	_	1.11	0.08
	2	_	1.01	0.20
	3	_	0.84	0.00
	Average		0.99	0.09

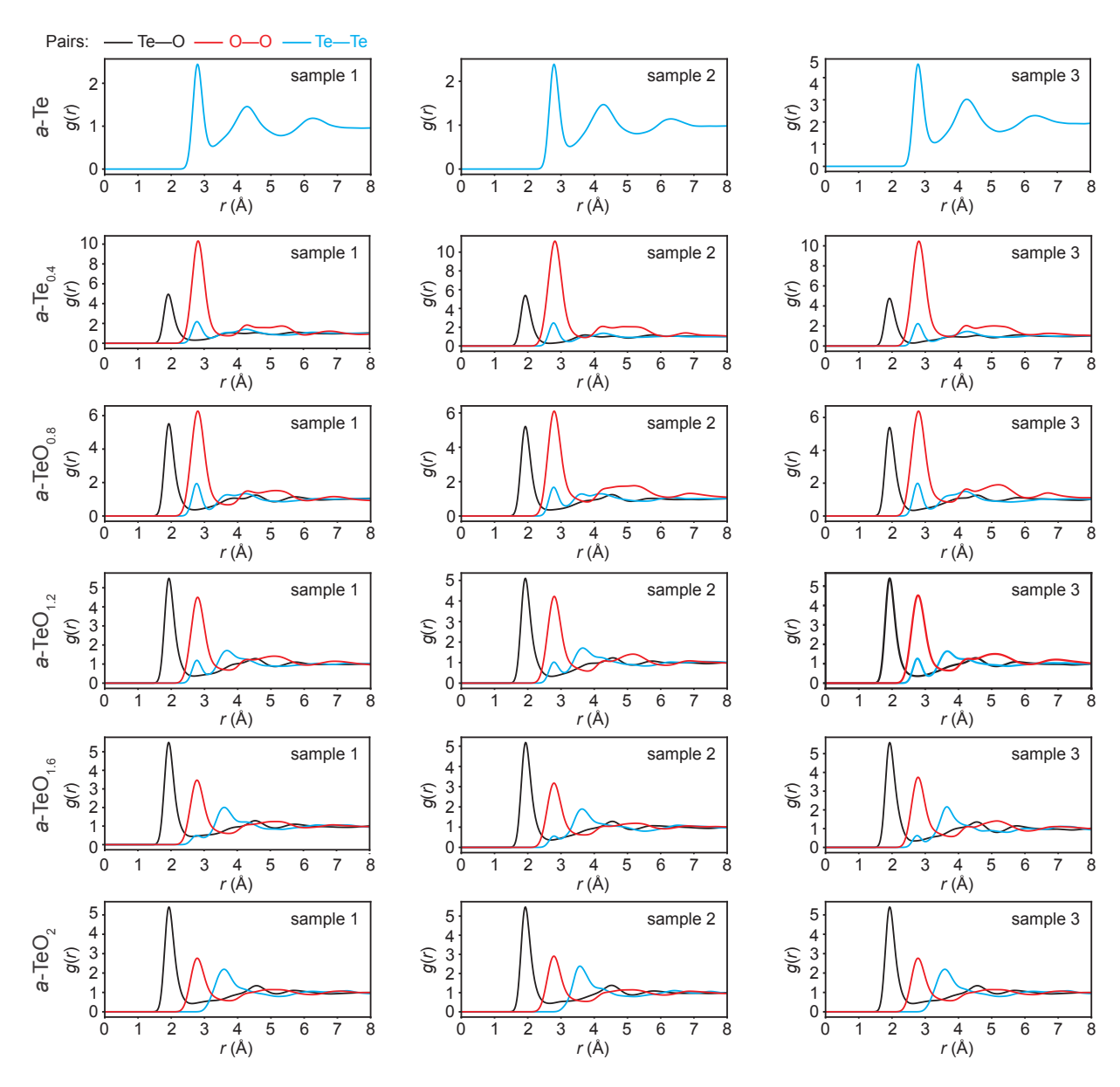


Figure S2: Pair-correlation functions, g(r), for Te–O (black), O–O (red), and Te–Te (blue) atom pairs, computed for independent amorphous samples at each composition from x=0 (a-Te) to x=2 (a-TeO₂). All structures were generated by ab initio melt-quench simulations under identical conditions. The systematic evolution of peak positions and intensities with oxygen content confirms the reproducibility and structural consistency across the compositional series.

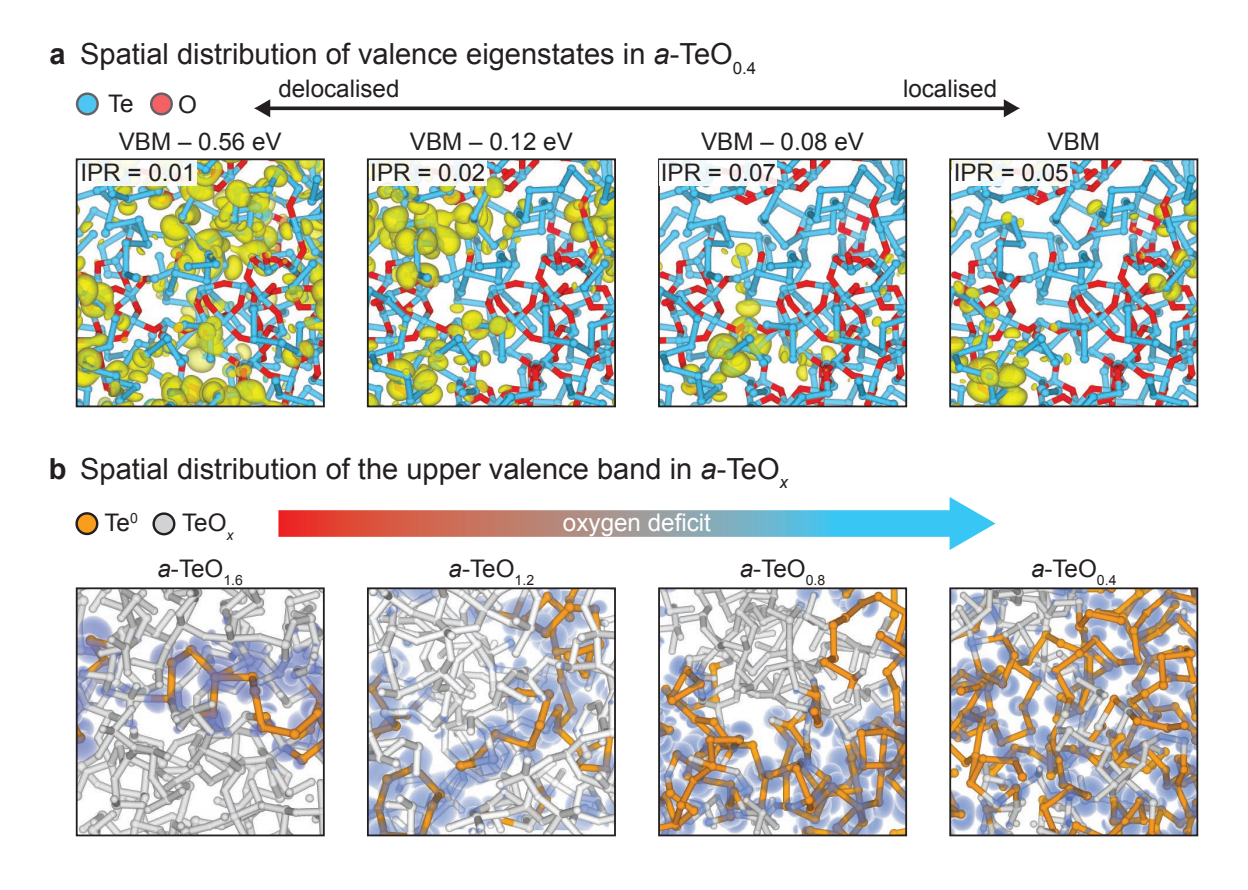


Figure S3: (a) Isosurface plots of selected valence-band eigenstates in a-TeO_{0.4}, shown with their energy relative to VBM and corresponding IPR. States with IPR < 0.03, deeper in the valence band, are typically delocalized. Yellow isosurfaces indicate the real-space distribution of the wavefunctions; Te and O atoms are shown in blue and red, respectively. (b) Real-space distribution of the upper valence-band states (in blue) across compositions from x=1.6 to 0.4, highlighting the transition from a percolative to a uniform network. The upper valence band, concentrated within the neutral Te-rich subnetwork (orange), progressively extends with decreasing oxygen content. The isosurface corresponds to the states within 0.5 eV below the valence band maximum (VBM), plotted at an isovalue of 5% of the maximum charge density.

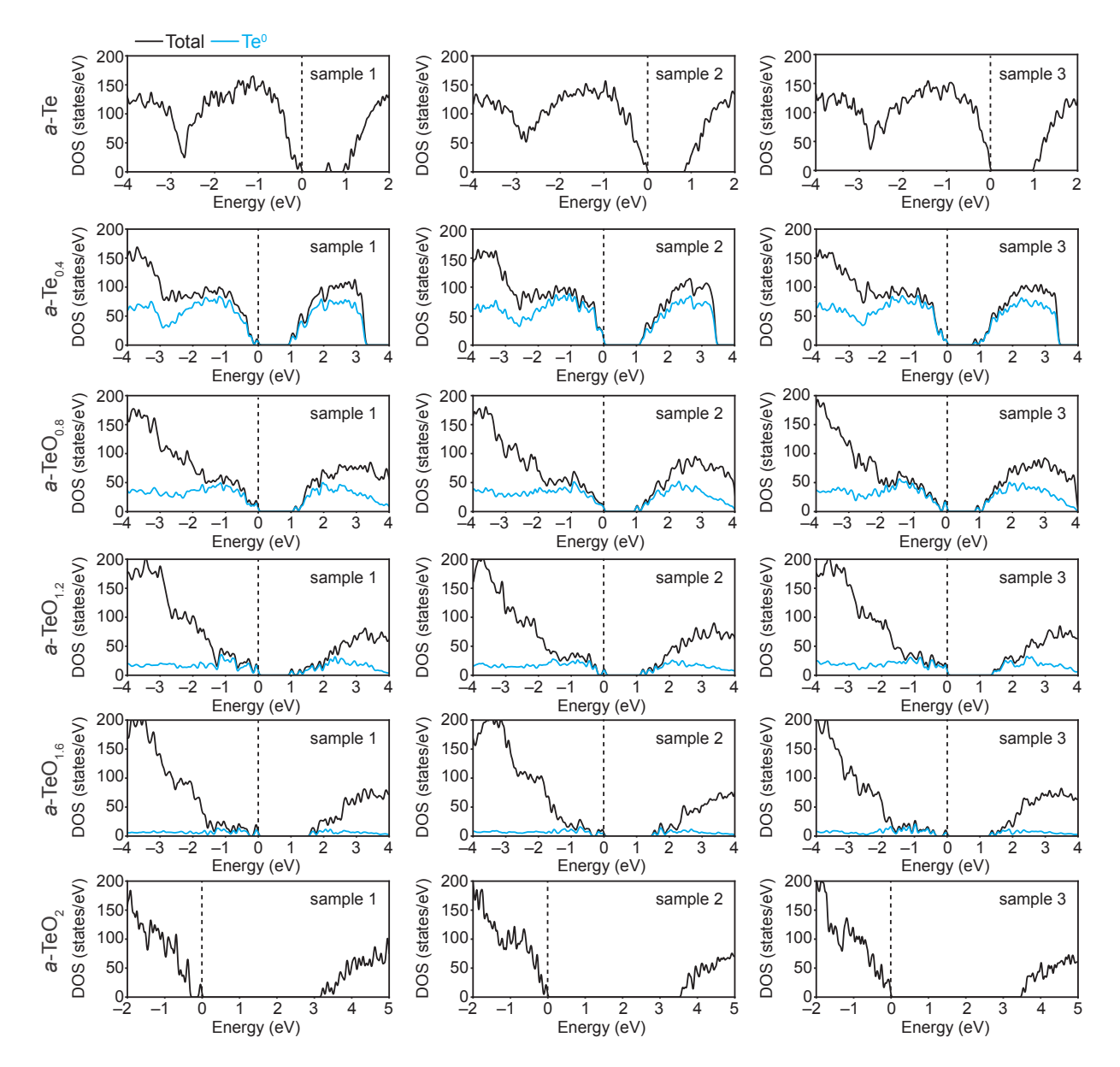


Figure S4: Total (black) and projected (blue) DOS for independent amorphous samples at each composition from x = 0 (a-Te) to x = 2 (a-TeO₂). The projected DOS corresponds to the contribution from neutral Te⁰ atoms. The energy is given relative to the valence band maximum (VBM), represented by the vertical dashed line. The evolution of the valence and conduction band edges with oxygen content reflects the transition from semimetallic to insulating behavior across the series.

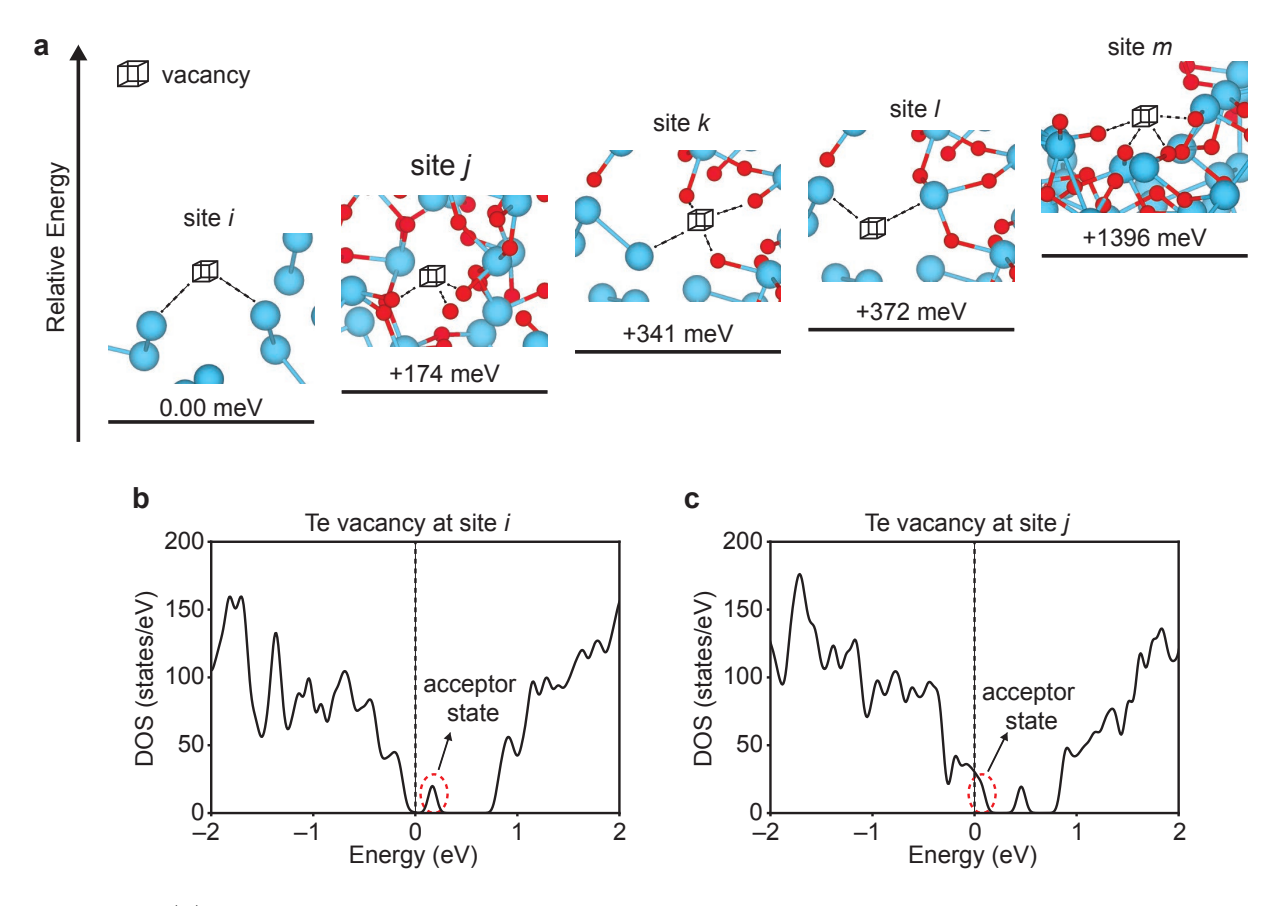


Figure S5: (a) Relative energies of tellurium vacancies introduced at five non-equivalent sites within an a-TeO_{0.8} model, highlighting the local bonding environments (Te: blue, O: red). Site i is the most stable configuration, while site m is over 1.3 eV higher in energy. (b,c) DOS for the Te vacancies at sites i and j, respectively, reveal the emergence of acceptor-like states just above the VBM, indicating the potential of Te vacancies as source of holes in oxygen-deficient samples. These results were obtained via r^2 SCAN functional.

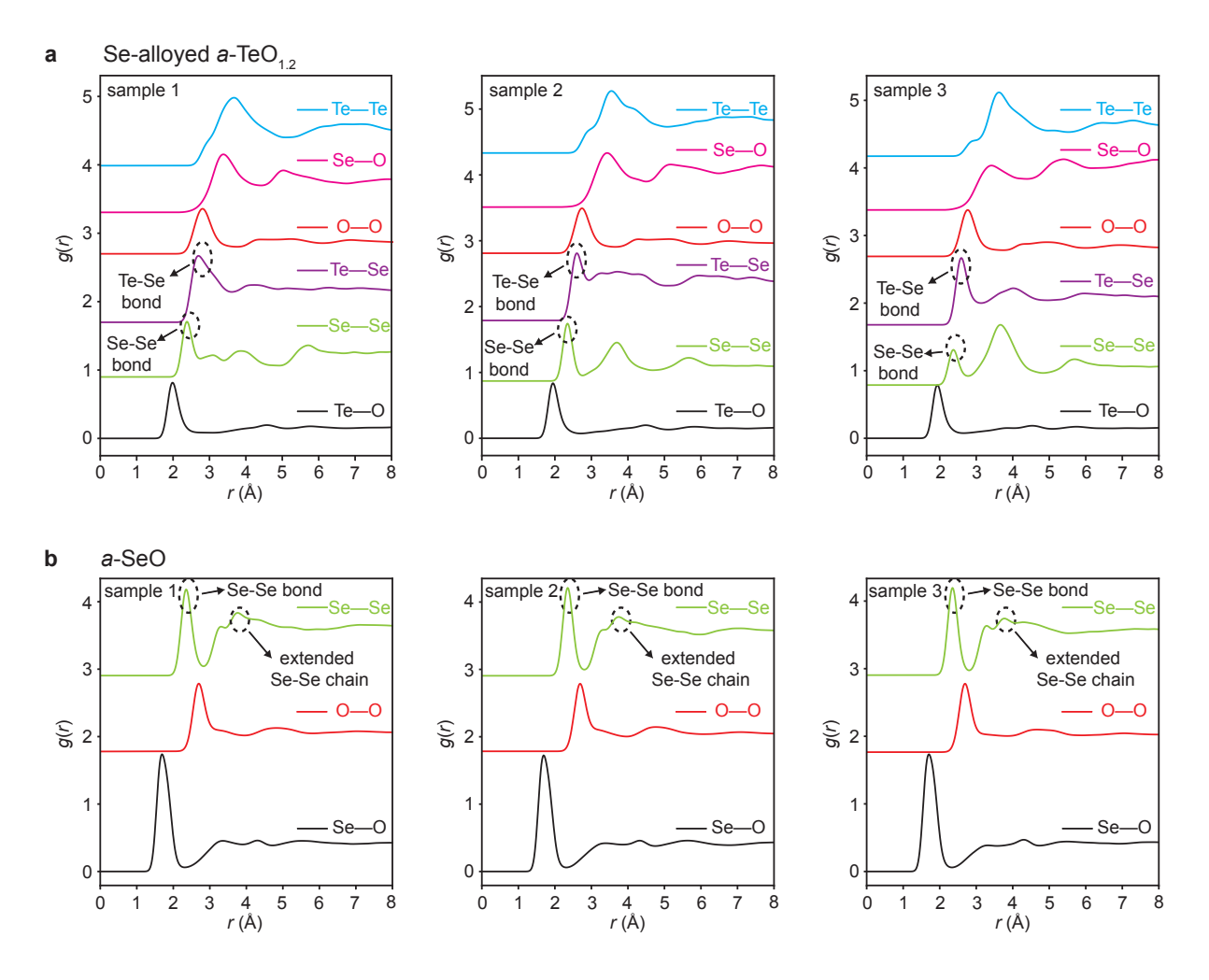


Figure S6: (a) Partial pair correlation functions g(r) for Se-alloyed a-TeO_{1,2} (Te:Se ratio 3:1), showing clear signatures of Te-Se and Se-Se bonds, along with the absence of direct Se-O bonding. (b) Corresponding g(r) for a-SeO, revealing both Se-Se bond and extended Se chain motifs. Dashed circles highlight the main interatomic correlations. Vertical offsets applied for clarity.

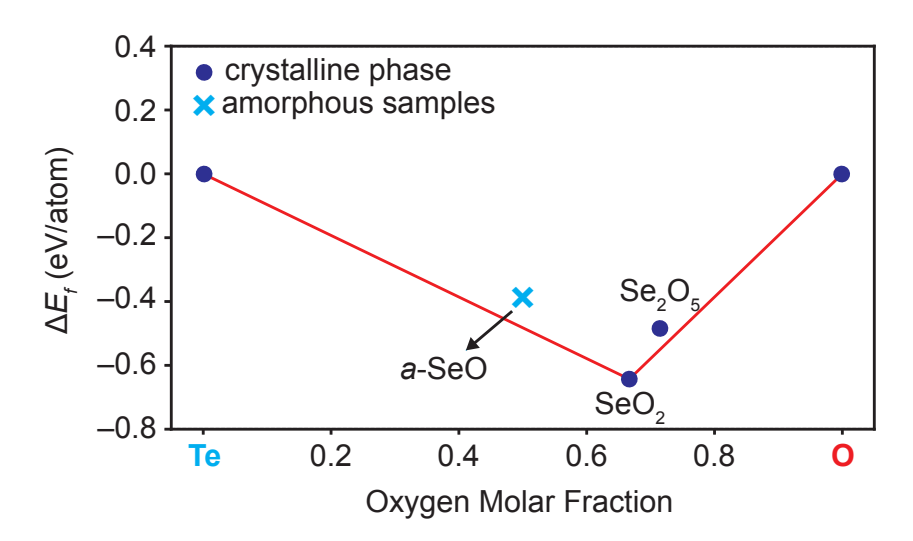


Figure S7: Formation energy convex hull, ΔE_f , for the Se-O binary system. Navy circles represent known crystalline phases on the convex hull, while blue crosses correspond to the simulated amorphous composition.

References

- Akola, J.; Jones, R. O. Structure and Dynamics in Amorphous Tellurium and Te_n Clusters: A Density Functional Study. *Phys. Rev. B* 2012, *85*, 134103, DOI: 10.1103/physrevb.85.134103.
- (2) Raghvender, R.; Bouzid, A.; Cadars, S.; Hamani, D.; Thomas, P.; Masson, O. Structure of Amorphous TeO₂ Revisited: A Hybrid Functional Ab initio Molecular Dynamics Study. Phys. Rev. B 2022, 106, 174201, DOI: 10.1103/physrevb.106.174201.
- (3) Heyd, J.; Scuseria, G. E.; Ernzerhof, M. Hybrid Functionals Based on a Screened Coulomb Potential. J. Chem. Phys. 2003, 118, 8207–8215, DOI: 10.1063/1.1564060.
- (4) Krukau, A. V.; Vydrov, O. A.; Izmaylov, A. F.; Scuseria, G. E. Influence of the Exchange Screening Parameter on the Performance of Screened Hybrid Functionals. J. Chem. Phys. 2006, 125, 224106, DOI: 10.1063/1.2404663.
- (5) Adenis, C.; Langer, V.; Lindqvist, O. Reinvestigation of the Structure of Tellurium. Acta Crystallogr. Sect. C 1989, 45, 941–942, DOI: 10.1107/s0108270188014453.
- (6) Loferski, J. J. Infrared Optical Properties of Single Crystals of Tellurium. Phys. Rev. 1954, 93, 707-716, DOI: 10.1103/physrev.93.707.
- (7) Lindqvist, O.; Haaland, A.; Nilsson, J. E.; Gronowitz, S.; Christiansen, H.; Rosén, U. Refinement of the Structure of alpha-TeO₂. Acta Chem. Scand. 1968, 22, 977–982, DOI: 10.3891/acta.chem.scand.22-0977.
- (8) Jain, H.; Nowick, A. S. Electrical Conduction in Paratellurite (TeO₂) Crystals. *Phys. Status Solidi A* **1981**, *67*, 701–707, DOI: 10.1002/pssa.2210670242.
- (9) Beyer, H. Verfeinerung der Kristallstruktur von Tellurit, dem Rhombischen TeO₂. Z. Kristallogr. Cryst. Mater. **1967**, 124, 228–237, DOI: 10.1524/zkri.1967.124.16.228.

- (10) Shi, J.; Zhang, J.; Yang, L.; Qu, M.; Qi, D.; Zhang, K. H. L. Wide Bandgap Oxide Semiconductors: from Materials Physics to Optoelectronic Devices. Adv. Mater. 2021, 33, 2006230, DOI: 10.1002/adma.202006230.
- (11) Champarnaud-Mesjard, J.; Blanchandin, S.; Thomas, P.; Mirgorodsky, A.; Merle-Méjean, T.; Frit, B. Crystal Structure, Raman Spectrum and Lattice Dynamics of a New Metastable Form of Tellurium Dioxide: γ-TeO₂. J. Phys. Chem. Solids 2000, 61, 1499–1507, DOI: 10.1016/s0022-3697(00)00012-3.
- (12) Dewan, N.; Sreenivas, K.; Gupta, V. Properties of Crystalline γ -TeO₂ Thin Film. J. Cryst. Growth 2007, 305, 237–241, DOI: 10.1016/j.jcrysgro.2007.03.054.
- (13) Lindqvist, O.; Moret, J. The Crystal Structure of Ditellurium Pentoxide, Te₂O₅. Acta Crystallogr. Sect. B **1973**, 29, 643–650, DOI: 10.1107/s0567740873003092.
- (14) Hoppe, R. The Coordination Number—an "Inorganic Chameleon". *Angew. Chem. Int. Ed.* **1970**, *9*, 25–34, DOI: 10.1002/anie.197000251.
- (15) Hirshfeld, F. L. Bonded-Atom Fragments for Describing Molecular Charge Densities. Theor. Chim. Acta 1977, 44, 129–138, DOI: 10.1007/bf00549096.
- (16) Da Silva, J. L. F. Effective Coordination Concept Applied for Phase Change $(GeTe)_m(Sb_2Te_3)_n$ Compounds. J. Appl. Phys. **2011**, 109, 023502, DOI: 10.1063/1.3533422.
- (17) Alderman, O. L. G.; Benmore, C. J.; Feller, S.; Kamitsos, E. I.; Simandiras, E. D.; Liakos, D. G.; Jesuit, M.; Boyd, M.; Packard, M.; Weber, R. Short-Range Disorder in TeO₂ Melt and Glass. J. Phys. Chem. Lett. 2019, 11, 427–431, DOI: 10.1021/acs.jpclett.9b03231.
- (18) Gulenko, A.; Masson, O.; Berghout, A.; Hamani, D.; Thomas, P. Atomistic Simulations

- of TeO₂-based Glasses: Interatomic Potentials and Molecular Dynamics. *Phys. Chem. Chem. Phys.* **2014**, *16*, 14150–14160, DOI: 10.1039/c4cp01273a.
- (19) Barney, E. R.; Hannon, A. C.; Holland, D.; Umesaki, N.; Tatsumisago, M.; Orman, R. G.; Feller, S. Terminal Oxygens in Amorphous TeO₂. J. Phys. Chem. Lett. 2013, 4, 2312–2316, DOI: 10.1021/jz4010637.
- (20) Marple, M. A.; Jesuit, M.; Hung, I.; Gan, Z.; Feller, S.; Sen, S. Structure of TeO₂ Glass: Results from 2D 125Te NMR Spectroscopy. J. Non-Cryst. Solids 2019, 513, 183–190, DOI: 10.1016/j.jnoncrysol.2019.03.019.
- (21) Ichikawa, T. Electron Diffraction Study of the Local Atomic Arrangement in Amorphous Tellurium Films. *Phys. Status Solidi B* **1973**, *56*, 707–715, DOI: 10.1002/pssb.2220560235.